VSEBINA – CONTENTS

IZVIRNI ZNANSTVENI ČLANKI – ORIGINAL SCIENTIFIC ARTICLES

THERMAL FATIGUE OF A Ni-BASED SUPERALLOY SINGLE CRYSTAL

TERMIČNA UTRUJENOST MONOKRISTALA IZ NIKLJEVE SUPERZLITINE

[1]Leonid Getsov, [2]Natalia Dobina, [2]Alexandr Rybnikov

[1]Department of Strength of Materials, St. Petersburg State Politechnical University, St. Petersburg, Russia
[2] NPO ZKTI, Russia
guetsov@online.ru

This paper presents a thermal-mechanical fatigue (TMF) test procedure and some results obtained in vacuum for a Ni-based superalloy single crystal. This procedure allows the monitoring of slip lines, fatigue-crack initiation and propagation until final failure. Single-crystal specimens with different crystallographic orientations were tested under different thermal-cyclic loading conditions. Tests were conducted on smooth specimens as well as on specimens with a central hole of 0.5 mm diameter to analyze the effects of stress concentration. Both crystallographic and non-crystallographic cracks were observed. An increase of the maximum temperature in the cycle (with the same amplitude of temperature change) causes a severe shortening of the service life, as well as stress concentration. It was observed that the first initiated microcrack arrests and the sample fracture takes place on newly nascent microcracks.

Key words: thermal fatigue, single crystal, crystallographic orientation, crack, concentrator

V članku je opisana procedura za določitev termičnega utrujanja (TMF) in nekateri rezultati preizkusov monokristala iz nikljeve superzlitine v vakuumu. Procedura omogoča opazovanje drsnih črt ter začetek in propagacijo razpok do končnega preloma. Monokristali z različno prostorsko orientacijo so bili preizkušani pri različnih pogojih termično ciklične obremenitve. Preizkusi so bili izvršeni na gladkih preizkušancih in na takih s centralno izvrtino s premerom 0,5 zaradi analize koncentracije napetosti. Opažene so bile kristalografske in rekristalografske razpoke. Povišanje najvišje temperature v ciklu (pri enakem razponu spremembe temperature) povzroči veliko skrajšanje uporabne dobe, enak je vpliv koncentracije napetosti. Ugotovljeno je bilo, da se prva mikrorazpoka ustavi in da prelom nastane zaradi novo nastalih mikrorazpok.

Ključne besede: termična utrujenost, monokristal, kristalografska orientacija, razpoka, koncentrator

1 INTRODUCTION

Thermal-fatigue crack initiation in single-crystal aerofoils is the major cause of damage during turbine operation. A detailed study of fatigue-crack initiation and growth has been made [1-5]. This paper describes a new thermal-cyclic vacuum test procedure. During vacuum testing, this procedure makes it possible to monitor the crystallographic slip orientations, crack initiation and growth.

The publications [8-12] present a detailed review of research on the strength of single-crystal superalloys, carried out on the basis of an analysis of the literature with most of the attention paid to the publications of Russian researchers and, in particular, the authors of this paper. The problems of the influence of the anisotropy of single-crystal superalloys on the parameters of fatigue and the thermal-fatigue strengths are considered; some basic phenomenological and physical models of the material for the calculation of the deformation mode in single crystals are described and the criteria of thermal-fatigue fractures are discussed. Different aspects of the initiation and the evolution of the creep, fatigue and thermal fatigue cracks in single-crystal materials are considered, and their dependence on the temperature parameters, crystallographic orientation and their

formation development mode was surveyed. Approaches to the definition of the fracture criteria and the methods of determining the deformation mode have been analyzed. Considerable attention is paid to the examination of the process of fatigue-crack development in single-crystals superalloys in the cases of HCF and LCF. The crystallographic peculiarities of fatigue failure and the criteria for the determination of the crack-growth direction and the rate at the different stages are considered. Special attention is paid to the conditions of the transition between stages.

2 EXPERIMENTAL PROCEDURE

2.1 Test procedure. A comprehensive procedure is developed in NPO CKTI for the determination of the thermal fatigue resistance of the various materials and coatings. A flat specimen is rigidly fixed in the vacuum chamber and cyclically heated with electric current (**Figure 1**). The heating is carried out according to the specified program (**Figure 2**) and automatically maintained during the testing. With the increase of the vacuum depth, the ultimate cycle temperature increases also. The temperature is measured with the rate of oxide-film formation on the sample surface. The slip
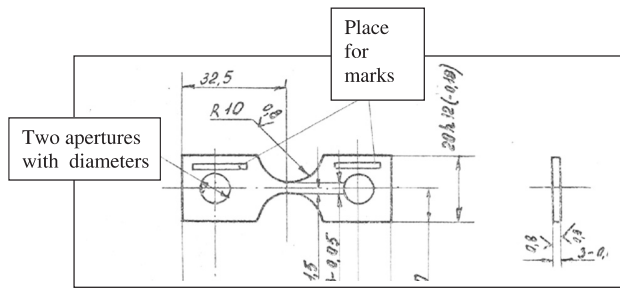
Figure 1: Specimen shape and size
Slika 1: Oblika in mere preizkušanca

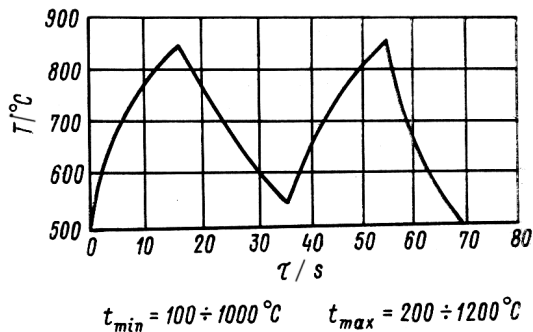$$t_{min} = 100 \div 1000 \,^{\circ}C \qquad t_{max} = 200 \div 1200 \,^{\circ}C$$

Figure 2: Program of the temperature-cycle variation
Slika 2: Program temperaturnega cikla

lines and surface microcracks are observed with an optical microscope [6].

The technique enables to:

- Determine the thermo-fatigue resistance for gas-turbine blades based on crack initiation and propagation.
- Compare of different material-processing techniques, parts manufacturing, repair and coating technologies by TMF resistance.
- Perform fatigue tests of small-scale specimens cut out from the gas-turbine blades after operation.
- To define the minimum thermal fatigue resistance of construction elements including composite materials, single-layer and multilayer coatings and welded joints.
- To study the details of the mechanism of thermal fatigue for material for various cycle parameters.
- To study the effect of stress concentration on the thermal fatigue.
- To determine crack orientations (ratio of $\Delta K_I/\Delta K_{II}$), the crack propagation rate, and the effect of the cycle's parameters on the crack propagation and on the thermal fatigue service life.

2.2 With testing the following parameters are determined: characteristic properties of the deformation relief defining the mechanism of thermal-fatigue damage accumulation; the number of cycles to the first appearance of the microcrack in the speciment and in the coating; the growth rate of incipient cracks and the number of cycles to sample failure.

The amplitude value of conventional elastic stresses is determined according to:

$$\Delta\sigma = (E_{st1}\alpha_1 T_{max} - E_{st2}\alpha_2 T_{min})\varphi$$
$$\varphi = 1 - \Delta k / \Delta l \qquad (1)$$

where Δk is the measured value of the displacement during the cycle of control micro-hardness marks, applied on the sample surface along its working part edges; E_{st} is a static module of elasticity; and Δl is the free movement of the control marks during the heating from T_{min} to T_{max}.

The stress-strain relationship and the inelastic deformation evolution are calculated using a structural model [7]. The specific feature of this procedure and those of Coffin are the constant stresses over the sample's cross-section.

The number of cycles to failure of flat samples in vacuum and of tube samples in air that were tested using the different test units of Coffin, under thermal cycle loading, turned out to be identical for a number of heat-resistant nickel-based alloys.

In this project tests were carried out under permanent visual surface observation and periodic photographing of the slip lines' orientation, the surface microcracks' initiation and the changes of the slip lines' orientation during thermal cycling with the optical magnification of 260 times. It should be noted that photographing during the course of the tests makes it possible to obtain high-quality images. TMF tests were conducted until failure or 2000 cycles, depending on which event happened first. After the tests the fracture surfaces were analyzed using optical fractography and a magnification of 160 times. Some tests were conducted on the samples with stress concentrators in the form of 0.5 mm holes.

2.3 Materials. The plates of the monocrystal alloy underwent the standard thermal treatment: heating in vacuum up to 1320 °C, holding at this temperature for 6 h, and cooling in argon. This was followed by double-stage aging in the mode: first stage, heating in air up to 1030 °C, holding at this temperature for 4 h; second stage, 24 h at 870 °C. The as-received crystal orientation is listed in **Table 1**.

Table1: Crystallographic orientation of single-crystal plates
Tabela 1: Kristalografska orientacija monokristalnih plošč

Number of the sample series	The crystallographic orientation of the samples along the longer axis	Deviation from exact orientation, degree	Azimuthal orientation, degree
1	[111]	5.64	8.26
2	[011]	4.51	11.27
3	[011]	8.33	14.43
4	[011]	9.67	7.86
5	[001]	5.47	41.97

3 RESULTS AND DISCUSSION

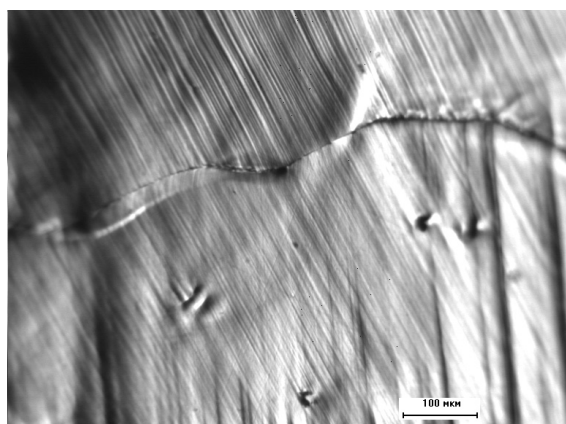Despite the limited number of tests, the obtained experimental data allow us to formulate some

relationships which, of course, require further experimental verification.

3.1 Directions of the slip lines. The analysis of the test data shows that for different crystallographic orientations the slip lines form under different angles, including those oriented approximately across and along the loading vector, and also at an angle close to 45°. We obtained a reasonably good convergence between the experimentally measured and predicted slip lines. For a small number of cycles the nascent slip lines are oriented in the directions corresponding to the greatest Schmid factor. It should be noted that in the samples of series 3, 4 and 5 (**Table 2**) the slip lines corresponding to both, the octahedral and cubic slip systems, were observed (**Figure 3**), and in the samples of series 1 and 2, only those corresponding to the octahedral system were seen (**Figure 4**). Multiple slip and even patchy appears with an increase in the number of cycles. Microcracks initiate mainly on slip lines, but the direction of their growth does not depend on the direction of the slip lines, therefore, it has a non-crystallographic nature. Thus, initially, the microcrack is parallel to the slip lines, and then the crack turns out to be oriented along the sample axis (maximum compression). It is worth noting that no slip lines were found in this direction. Also, non-crystallographic directions of microcracks were observed in the micrographs of the fracture zones of all the samples (see **Figure 5**).

3.2 Orientation of the fracture surface

The character of the sample fracture can be seen in the scheme of **Figure 6** and the picture in **Figure 7**. The directions of the distribution of cracks were compared to the directions of the sliding lines.

The samples 3-0, 3-1, 3-3 of the series 3 [011] broke mainly in a zigzag line in the lattice plane, the samples 3-2, 3-4, 3-5 ruptured in the plane. At the upper edge of the section, the samples 3-0 and 3-5 were damaged by

the rupture and the samples 3-1, 3-2, 3-3, 3-4 were damaged below the edge.

Table 2: Comparison of the calculated and experimental directions of the slip lines
Tabela 2: Primerjava izračunanih in eksperimentalnih smeri drsnih črt

Sample number	Exp. slip line slope [deg.]	Theor. slip line slope	
		octahedron	cubic
2-1	**10**	**6.1**	-
	80; 82.5; 76.8; 78; 78.2; 82; 83; 84.2	81	-
	93	95.8	-
2-2	**75.8; 80.5;88.8; 86**	81	-
		-	-
	99	95.8	-
	114;126	-	132.8
2-4	**0; 1.3**	**0.2**	-
	84.5	81	-
2-6	**4.2; 3.8**	**6.1**	-
	79.8; 81.2; 82; 85.8	81	-
	93.5; 95.5	95.8	-
5-1	93.2	90.2	95.5
5-2	**3.5**	-	**5.3; 5.6**
	92.6	90.2	**95.5**
	107.1	100.2	-
5-3	**39.4**	**40.8**	-
	90.6	90.2	-
	149	150.2	-
1-6	**17.8**	**16.5**	-
	131.2	130	-
1-2	**22.4; 20.8**	**16.5**	-
	130.5	130	-
1-1	**15.8**	**16.5**	-
	83.2; 82.5	87.5	-
	128.5; 130.8	130	-
3-0	**15**	-	**14.8**
	85	93.6	-
	170.174	175.7	
3-1	**70.5**	**74.8**	
	89	93.6	
3-2	**35**	-	**38.6**
	71.5	74.8	
	93.2	93.6	
3-3	**91; 95.5**	**93.6**	
	169.2	167.5	
3-4	**21; 22.5**	-	**14.8**
	65.5	74.8	
	93.2; 92.5; 92	93.6	
4-1	**50**	**48.8**	-
	78.5	163.2	83.8; 84.9
	155; 154; 162.4; 158.5		-
4-2	**48.1; 51.2; 49.2; 48.5**	**48.8**	-
		-	**83.8; 84.9**
	86.5; 81.5		

Figure 3: Microstructure of the surface of specimen 3-2 after 63 cycles (250–1000 °C)
Slika 3: Mikrostruktura površine preizkušanca 3-2 po 63 ciklih (250–1000 °C)
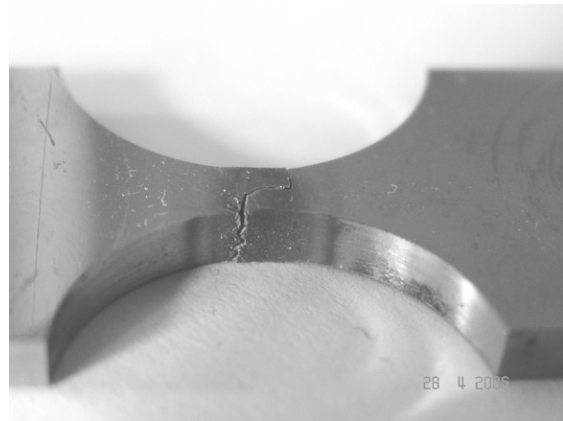
Figure 4: Microstructure of the fractured specimen 5-3
Slika 4: Mikrostruktura prelomljenega preizkušanca 5-3

Figure 6: Appearance of the fractured specimen 3-0
Slika 6: Prelomljen preizkušanec 3-0
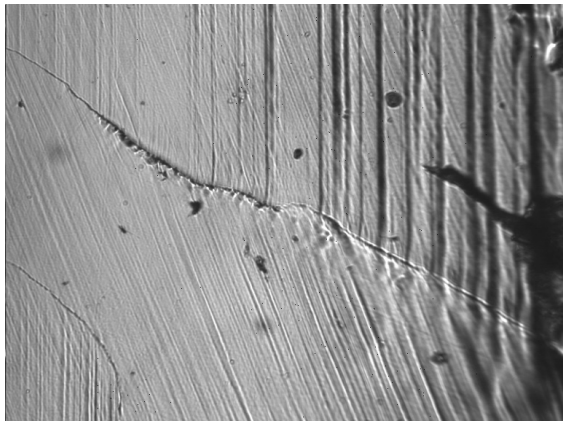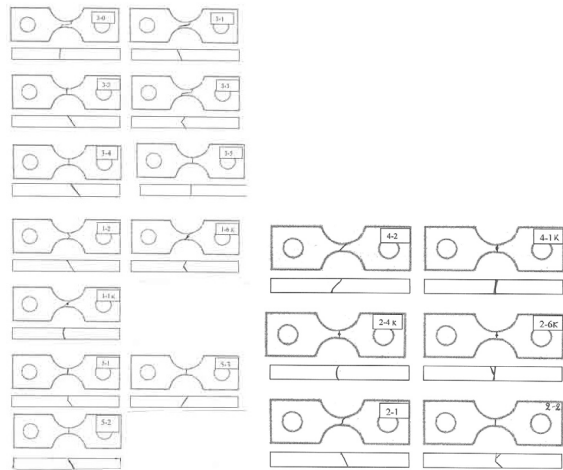

Figure 5: Microstructure in the vicinity of the fracture of specimen 3-2
Slika 5: Mikrostruktura v bližini preloma vzorca 3-2

Figure 7: Course of the fracture lines in the specimens
Slika 7: Potek razpok v preizkušancih

The samples of series 5 [001] broke perpendicularly to the loading vector along the lattice plane and at the angle toward the specimen plane (shear).

The samples 2-4 and 2-6, with concentrator of series 2 [011], broke perpendicularly to the loading vector along the plane and on the specimen plane. The sample 2-1 without a concentrator broke by shear in the plane and on the section.

The sample 4-1 of series 4 (with mixed orientation) with the concentrator was fractured perpendicularly to the loading vector, and the smooth sample 4-2 cracked at an angle toward the specimen axis and plane (shear).

The samples of series 1 [111] with and without a concentrator cracked by shear with a change of direction in the surface and in the section.

Table 3: Influence of the maximal temperature of a cycle on the number of total cycles to failure
Tabela 3: Vpliv najvišje temperature v ciklu na število ciklov do preloma

Sample number	Orientation	ΔT	$T_{min}/°C$	$T_{max}/°C$	N
3-0	011	750	150	900	951
3-1			200	950	450
3-2			250	1000	63
3-5		500	450	950	2535
3-3			500	1000	1220
3-4			550	1050	356
5-1	001	750	150	900	560
5-2			250	1000	95
2-4 with stress concentrator	011	500	350	850	2952
2-6 with stress concentrator			500	1000	187

3.3 Influence of the maximum temperature in the cycle

The data in **Table 3** show that the increase of the maximum temperature within the ranges 850–1000 °C and 900–1000 °C with the same total temperature amplitude decreases the service life to fracture by ≈ 15 times. If the maximal temperature is increased from 1000 °C up to 1050 °C with the same total temperature amplitude the time-to-fracture is decreased by approximately a factor of 4.

3.4 Influence of the total temperature amplitude

A decrease of the total temperature amplitude with a constant value of $T_{MAX} = 1000$ °C increases considerably the service life (**Table 4**).

Table 4: Influence of the temperature range on the number of cycles to fracture
Tabela 4: Vpliv razpona temperature v ciklu na število ciklov do preloma

Sample number	Orientation	T_{min}/°C	T_{max}/°C	N
3-2	011	250	1000	63
3-3	011	500	1000	1220
5-2	001	250	1000	95
5-3	001	500	1000	1460

3.5. Influence of the stress concentrator

Concentrators in samples in the form of holes with a diameter of 0.5 mm decrease the service life by ≈ 15 times (**Table 5**). At the same time, during the test of the sample with the concentrator and $T_{max} = 850$ °C a relatively large number of cycles before fracture (2952) was recorded. The sample without concentrator was not tested in such conditions, since the expected number of cycles before the fracture occurred was more than 10000.

Table 5: Influence of the stress concentrator on the number of cycles before destruction.
Tabela 5: Vpliv koncentratorja napetosti na število ciklov do preloma

Sample number	4-2	4-1 with stress concentrator	1-2	1-1 with stress concentrator	2-2	2-6 with stress concentrator
Orientation	[011]	[011]	[011]	[011]	[011]	[011]
T_{min}/°C	150	150	150	150	500	500
T_{max}/°C	900	900	900	900	1000	1000
N	308	25	823	50	472	187

3.6 Influence of the crystallographic orientation of material

The maximal thermal fatigue life in tests under the same thermal cycle modes was observed in the case of smooth samples with a [111] orientation and the minimal strength was obtained for the [011] direction (**Table 6**). Samples with a mixed orientation and [001] broke after a number of cycles decreasing in the series $N_{111} > N_{001} > N_{mix} > N_{011}$. At the same time, the notched samples with orientation [011] had a longer life than the samples with the orientation [111]. The reasons for such behavior require further research. The influence of the azimuthal orientation of single-crystal alloys [011] on the number of cycles before destruction is illustrated by the data in **Table 7**.

Table 6: Influence of orientation on the number of cycles before destruction.
Tabela 6: Vpliv orietacije na število ciklov do preloma

Sample number	Orientation	T_{min} /°C	T_{max}/°C	N
2-1	[011]	150	900	100
4-2	[011]			308
1-2	[111]			823
5-1	[001]			560
3-2	[011]	250	1000	63
5-2	[001]			95
2-2	[011]	500	1000	472
3-3	[011]			1220
5-3	[001]			1460
2-4 with stress concentrator	[011]	350	850	2952
1-6 with stress concentrator	[111]			320

Table 7: Influence of the azimuthal orientation of single-crystal alloys [011] on the number of cycles before destruction ($T_{min} = 150$ °C, $T_{max} = 900$ °C)
Tabela 7: Vpliv azimutne orientacije monokristala [011] na število ciklov do preloma ($T_{min} = 150$ °C, $T_{max} = 900$ °C)

Sample number	A deviation from exact orientation, degree	Azimuthal orientation, degree	N
2-1	4.51	11.27	100
3-0	8.33	14.43	951
4-2	9.67	7.86	308

Figure 8: Microstructure of the surface of specimen 3-0 after 100 cycles (150–900 °C)
Slika 8. Mikrostruktura površine preizkušanca 3-0 po 100 ciklih (150–900 °C)

On of the samples the initiation of several micro-cracks, was observed often (but not always) oriented along the slip lines; some of the cracks originated near the pores. However, the fracture, as a rule, occurred from cracks located at some distance from the first micro-crack.

3.7 Influence of the recrystallization

The recrystallization on sample 3-0 with the [011] crystallographic orientation hindered the development of slip lines. The microcrack initiation was observed on the sample surface beside the recrystallization areas (**Figure 8**). Nevertheless, these microcracks did not evolve into macrocracks and the sample fracture had a complex trajectory after a large number of cycles.

4 CONCLUSIONS

Within the framework of this project ingot blanks of single-crystal superalloys with five different crystallo-graphic orientations were investigated. A new testing technique was developed, allowing obtain data on the role of the maximal and minimal cycle temperature, the stress concentration and the crystallographic orientation on the formation of slip lines, of microcracks and their propagation. On the basis of 18 tests with a maximum number of cycles equal to 2952 in the temperature range $T_{min} = 150$–500 °C, $T_{max} = 850$–1050 °C it was found that the thermal fatigue-crack initiation and growth are strongly influenced by the crystallographic orientation. Nevertheless, the fracture proceeds in a non-crystallo-graphic mode and in some cases the cracks change their direction of propagation.

The following conclusions are proposed:

1. It was observed that the sample fracture takes place, depending on the orientation and the test mode, both in crystallographic and non-crystallographic directions independently of the crystallographic slipping.
2. Different directions of slip in different sections of the sample surface were discovered, including multiple slip.
3. A sharp reduction in fatigue life was observed with an increase in the maximum temperature in the cycle (with the same amplitude of temperature change).
4. The stress concentrators decrease significantly the fatigue life.
5. It was observed that the initial microcrack decelerates and stops and the sample fracture takes place on a newly nascent microcrack.

In the authors' opinion it would be useful to carry out further research, focusing on the detailed study of the fractured samples and thermal fatigue tests, keeping the samples at the maximum temperature for the same time interval in each cycle. Further study of the problem of the thermal fatigue strengths of the blades should concentrate on the development of computational methods for the deformation mode of single-crystal blades by creep and cyclic change of temperature, on the estimation of the blades' strength for thermal-cycle loading and on the development of a method for calculating the crack-growth rate, taking into account creep, stress concentration and fracture-mode changes.

Acknowledgement

5 REFERENCES

[1] P. A. S. Reed, X. D. Wu, Sinclair Fatigue crack path prediction in UDIMET 720 nickel-based alloy single crystals. Metallurgical and Materials. 31A (**2000**), 109–120

[2] J. Telesman , L. J. Ghosn. Fatigue crack growth behavior of a PWA 1484 single crystal superalloy at elevated temperatures. ASME Paper 95-GT-452, 1995

[3] K. S. Chan, J. Feiger, Y.-D. Lee, R. John, S. J. Hudak. Fatigue crack growth thresholds of deflected mixed-mode cracks in PWA1484, Journal of Engineering Materials and Technology. 127 (**2005**), 2–7

[4] S. X. Li, D. J. Smith, An overview of combined fatigue and creep response of single crystal nickel base superalloys. Proc. 5-th Liege Conf. on Materials for Advanced Power Engineering, Part II, October, 1974, Belgium, 1175–1184

[5] N. Marchal, S. Forest, L. Remy, S. Duvinage. Simulation of fatigue crack growth in single crystal superalloy using local approach to fracture. Euromech- mecamat 2006, Local approach to fracture, 9-12 May 2006

[6] A. I. Rybnikov, L. B. Getsov. New technique and results of ther-mal fatigue tests of superalloys and coatings. Proceedings of the sixth International Congress on Thermal Stresses. Vienna, Austria, 1 (**2005**), 305–309

[7] L. G. Padva, L. B. Getsov, O. S. Sadakov, A. I. Rybnikov Design method of strength estimation for gas turbine blades with coatings, Journal of Machinery Manufacture Under Reliability Problem, 4 (**1992**), 57–63

[8] Golubovskiy E., Svetlov I., Nozhnitsky Yu. Relationship of stress rupture and crystallographic orientation for Ni-base superalloys single crystal. EUCASS. European Conference for Aerospace Sciences. July 4-7, 2005, Moskow, Russia, CD

[9] Rtishchev V. V. Anisotropic alloys with columnar and single crystal structures used for blades of stationary gas turbine plants. Proc. 5th Liege Conf. on Materials for Advanced Power Engineering, Part II, October, 1994, Belgium, 1135–1144

[10] R. E. Shalin, I. L. Svetlov, E. B. Kachanov et al.: Single crystal nickel base superalloys, Mashinbuilding, (**1997**) 333 (In Russian)

[11] Erickson G. L., Harris K. Ds and sx superalloys for industrial gas turbines, Proc. 5th Liege Conf. on Materials for Advanced Power Engineering, Part II, October, 1994, Belgium, 1055–1074

[12] Jo C.-Y., Kim H.-M. Effect of recrystallisation on microstructural evolution and mechanical properties of single crystal nickel based superalloy CMSX-2 Part 2 – Creep behaviour of surface recry-stallised single crystal., 19 (**2003**) 12, 1671–1676

NUMERICAL DETERMINATION OF THE CARRYING CAPACITY OF ROLLING ROTATIONAL CONNECTIONS

NUMERIČNA DOLOČITEV NOSILNOSTI VTRLJIVIH KOTALNIH ZVEZ

Robert Kunc, Andrej Žerovnik, Matej Žvokelj, Ivan Prebil

Faculty of Mechanical Engineering, University of Ljubljana, Aškerčeva ul. 6 1000 Ljubljana, Slovenia
robert.kunc@fs.uni-lj.si

The exploitation of large axial bearings includes load peaks, which cause permanent deformation of the rolling contact. The plastic strain of the base material under the hardened rolling layer starts to grow and micro-cracks on the edge of the hardened layer and the peeling of this layer may occur. In our computation we have used an elasto-plastic model that combines isotropic and kinematic hardening and the growth of material damage. The damage model allows us to follow the variation of the elastic and plastic stress and deformation as a function of the number of cycles. In the article, an experimental verification of the described numerical model is shown, which can be used to determine the actual carrying capacity of the rolling contact for low-speed axial bearings.

Key words: rotational connections, low cycle fatigue, cyclic plasticity, damage

Pri uporabi velikih aksialnih ležajev se pojavljajo preobremenitve, ki povzročijo trajno deformacijo ležajnega kontakta. Plastična deformacija osnovnega materiala pod utrjeno ležajno površino začne rasti in lahko nastanejo mikrorazpoke na robu kaljene plasti ter njeno luščenje. Pri našem izračunu smo uporabili elastoplastični model, ki kombinira izotropno in kinematsko utrjevanje ter rast poškodovanosti materiala. Ta model omogoča sledenje spremembe elastoplastične napetosti in deformacije kot funkcijo števila ciklov. V članku je opisana eksperimentalna verifikacija opisanega numeričnega modela, ki ga lahko uporabimo za določitev prave nosilnosti ležajnega spoja za aksialne ležaje, ki delujejo pri majhni hitrosti.

Ključne besede: vrtljiva zveza, malociklična utrujenost, ciklična plastičnost, poškodbe

1 INTRODUCTION

Bearings are among the most frequently used elements in machine engineering. Owing to their widespread use, the requirements that a bearing must meet are highly diverse. Bearing use ranges from applications in which a bearing collapse does not constitute a major problem, to applications where the collapse of a bearing could lead to enormous economic losses and potentially disastrous consequences for people. The large bearings used in rolling rotational connections are an example of such an application.

The basic element of a rotational connection is a large rolling bearing, with attachment holes in the bearing rings, and a gear wheel (**Figure 1**). Alloyed steels such as 42 CrMo 4 and C 45 – ISO 683/1 are normally used in the production of bearing rings since the process requires thermal and mechanical treatments. The raceway is surface-hardened to attain the minimum hardness necessary to prevent the pressing-in of the rolling element. The actual external load and the elasticity of the upper and support structures cause an uneven distribution of the external loads over the rolling bearing's diameter [1-3]. This leads to local plastic deformations of the bearing raceway and to the initiation of damage, largely conditioned by the load size and material fatigue [4-5]. The existing models for determining the carrying capacity of large rolling-bearing conne-

ctions with surface-hardened raceways do not fully consider or even greatly simplify the actual state of the bearing ring [3-12].

In analyzing the actual carrying capacity of rolling contacts in large rolling bearings with surface-hardened raceways we have decided to use a combined elasto-plastic constitutive model, which links the material
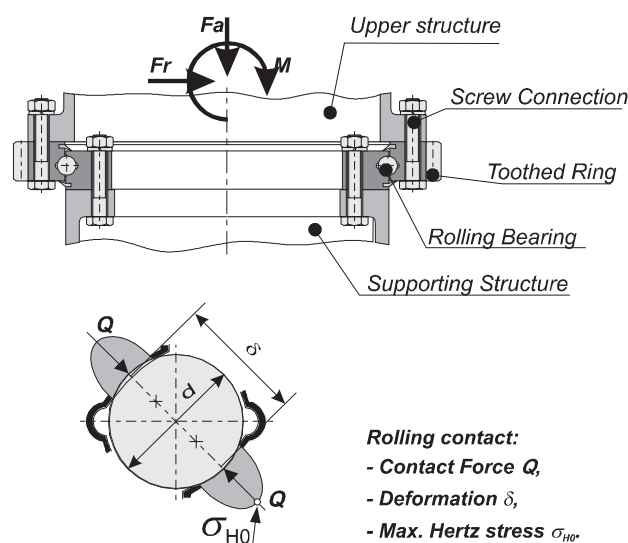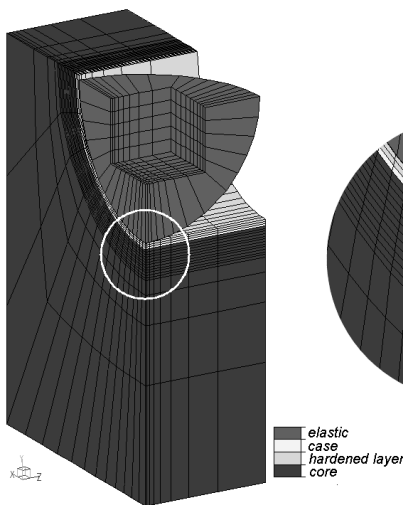

Figure 1: Elements of rotational connections
Sllika 1: Elementi rotacijskih povezav

damage mechanics with the isotropic and kinematic hardening/softening [13-15]. The material model considers 17 material parameters, selected from a series of monotone and cyclic experimental tests. The model, which was built in the finite-element code, was used to investigate the development of elasto-plastic deformations, stress areas and damage occurrence for low-cycle loads that occur in the raceways of large rolling bearings at a low rotational speed. In the article an experimental verification of the described numerical model is shown, which can be used for the determination of the actual carrying capacity of the rolling contact in low-speed axial bearings.
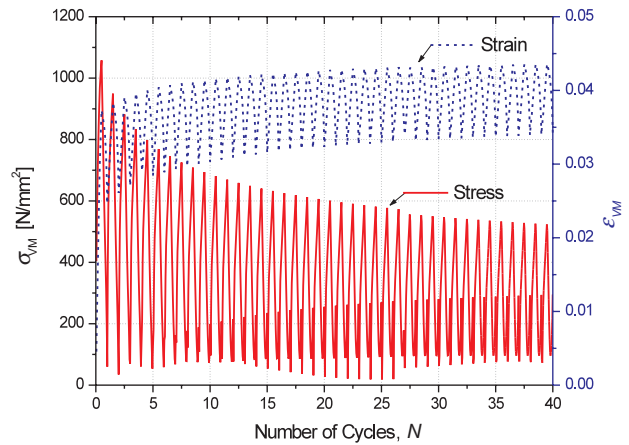
2 NUMERICAL MODEL

A developed and built-in finite element is used in the application of a numerical model focusing on the rolling contact between a raceway model and a rolling element, and is carried out in the ELFEN© commercial software environment. The discretisation of a bearing raceway's geometric model applies a developed finite element that covers isotropic hardening/softening, kinematic hardening and material damage [13-15]. This makes it possible to monitor the actual low-cycle development of the strain deformation or the hardening/softening and material damage growth. The end code of a developed element is written in the FORTRAN programming language. The geometry of the contact between the rolling element and the raceway is determined with square surface-contact elements (**Figure 2**).

The numerical model of a rolling contact considers the actual geometrical and material characteristics of bearing raceway models. The characteristics of a bearing ring model change in line with the raceway depth. After having measured the changes in hardness along the cross-section of a bearing raceway model, we entered various material parameters into the damage model.


Figure 3: Development of the stress σ_{VM} and strain ε_{VM} paths on the edge of the raceway-model hardened layer
Slika 3: Razvoj napetosti σ_{VM} in deformacije ε_{VM} na robu utrjene plasti ležajne tečine

These parameters were derived from the results obtained from single-axis monotone and cyclic tear tests [13]. In describing the material characteristics of raceway models, we also took into account the remaining material stresses that occurred during the production of the test raceways [14].

3 NUMERICAL RESULTS

The numerical rolling-contact model was used to simulate a contact of the rolling element and a surface-hardened bearing raceway at a varying contact force from F_{max} = 35.2 kN to F_{min} = 1 kN. The model enables every element to be assigned its deformation strain state and growth of damage relative to the number of contact load cycles. **Figure 3** shows the evolution of the equivalent von Mises stresses σ_{VM} and strains ε_{VM} at the location of maximum-damage accumulation for the first 40 loading cycles, and **Figure 4** shows a distribution

Figure 2: Numerical model
Slika 2: Numerični model
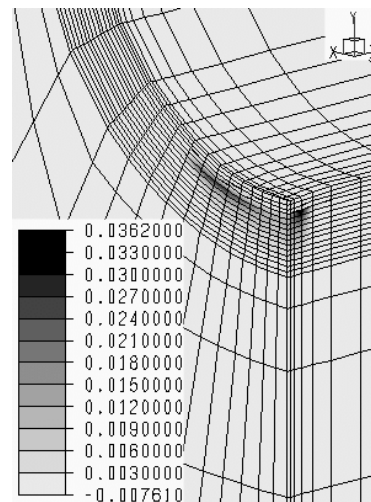
Figure 4: Damage distribution in 3D model after 100 load cycles
**Slika 4:** Porazdelitev poškodbe v 3D-modelu po 100 nihajih
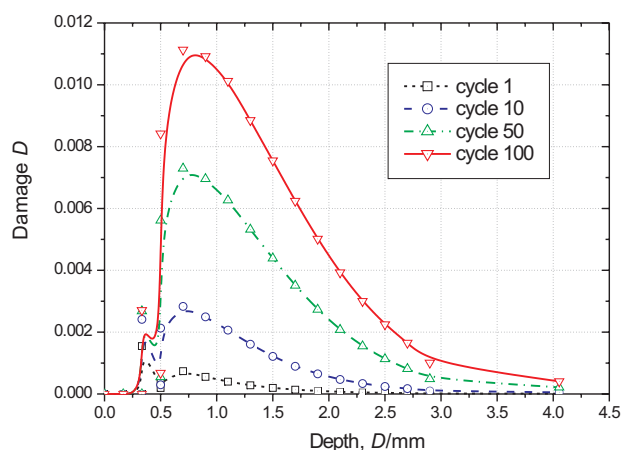
Figure 5: Damage distribution in ring depth
Slika 5: Porazdelitev poškodbe v globino ležajnega obroča

of the damage after 100 contact force cycles. In contrast, **Figure 5** shows the damage distribution along the ring depth that determines the damage accumulations in the base material on the edge of a hardened layer. The carrying capacity of the raceway model for rolling elements of different diameters was determined on the basis of a diagram showing the growth of material damage relative to the number of load cycles (**Figure 5**)[14].

4 VERIFICATION OF THE MODEL

A comparison of the results of the experimental work and the numerical calculations of the contact between the raceway model and the rolling element can only be made by comparing the directions of the maximum total and permanent displacements of the bearing-raceway model. The comparison shows an even development of the raceway-model displacements and thus supports the use of the proposed mechanical and mathematical models to
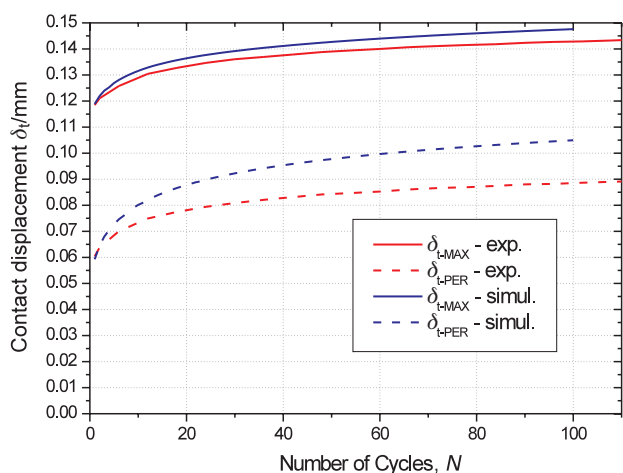
Figure 6: Comparison of the development of measured and calculated total and permanent displacements of the raceway-model damage distribution
Slika 6: Primerjava razvoja izmerjenega in izračunanega skupnega in permanentnega pomika za porazdelitev poškodbe ležajne tečine
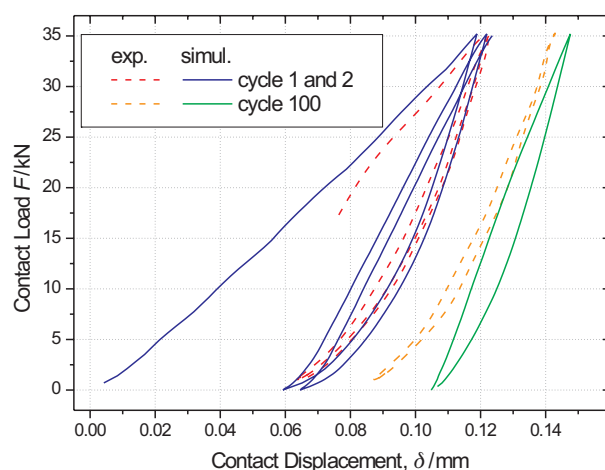
Figure 7: Comparison of the development of the measured and calculated displacement-contact force hysteresis of the raceway-model damage distribution
Sllika 7: Primerjava razvoja izmerjene in izračunane histereze v kontaktni sili za porazdelitev poškodbe ležajne tečine

determine the carrying capacity of large rolling bearings. There is a close match for the initial values of the measurements and the numerical calculations of the total and permanent displacement of the bearing raceway (**Figure 6**).

The matching is also evident from the comparison of the results obtained from measurements and numerical calculations of the first displacement-contact force hysteresis loop (**Figure 7**). Even when they are subjected to different loads and different geometric contact models, the measured and the calculated results of the total and permanent raceway displacements, which depend on the number of cycles, match closely their initial value and the deformation growth gradient [14].

5 CONCLUSION

The determination of the low-cycle carrying capacity of a large bearing raceway with the numerical model material behavior, which is applied with the finite-element method, is very effective. The model takes into account the geometric and construction characteristics of the bearing rings, the raceways, and the rolling elements as well as the material characteristics of the surface-hardened raceways, which link the continuum damage dynamics with the isotropic and kinematic hardening/softening. With regard to the expected loads and the geometric limitations of the rotational connection, both the geometry of the contact between the raceway and the rolling element as well as the heat treatment of the bearing rings can be optimized. We can also assess the life expectancy of a rotational connection, i.e., the time and location of the initiation of the macro-cracks on the surface-hardened bearing raceway.

Further investigations into the carrying capacity of a surface-hardened bearing raceway are focused on the

possibility of upgrading the material model with a rheological model for a description of the natural limits of the material yield, which occurs in the normalized and optimized bearing-ring base material, and with a model to describe the growth of a crack and the life expectancy of heat-treated steels used for bearing raceways.

6 REFERENCES

[1] J. Brandlein, Lastubertragung durch Grosswalzlager bei elastichen Ringtragern als Unter- und Oberkonstruktion, *f+h – Fordern und Heben*, 30, (**1980**)

[2] I. Prebil, S. Zupan, P. Lučič, Lastverteilung auf Wälzkörper der Drehverbindungen. *Konstruktion,* 47 (**1995**), 339–345

[3] E. V. Zaretsky, STLE Life Factors for Rolling Bearings, Chapter 4 – Bearing Load, STLE Publications, Illinois, 1992

[4] T. A. Harris, Rolling bearing analysis – 3rd edition, John Willey & Sons, New York, 1991

[5] R. A. Pallini, J. E. Sague, Computing core-yeild limits for case-haredened rolling bearings, ASLE Trans., 28 (**1985**) 1, 91–96

[6] J. E. Sague, The special way big bearings can fail, *Machine Design*, 50 (**1978**) 21, 113–120

[7] P. C. Bastias, Analysis of cyclic crack growth under rolling contact loading condition, Vanderbilt University, Dissertation, 1989

[8] ISO 281, Rolling bearings – Dynamic load ratings and rating life, 1990

[9] C. P. Jones, W. R. Tyfour, J.H. Beynon, A. Kapoor, The effect of strain hardening on shakedown limits of pearlitic steel, *Proc. Instr. Mech. Engrs*., 211 (**1997**), 131–140

[10] G. Lundberg, H. Sjovall, Stresses and deformation in elastic contacts, Chalmers University of Technology, Gothenburg, 1958

[11] H. R. Thomas, V. A. Hoersch, Stresses due to the pressure of one elastic solid upon another, University of Illinois, 212 (**1930**)

[12] G. Rydholm, On inequalities and shakedown in contact problems, Department of Mechanical Engineering, Linkoping University, 1981

[13] R. Kunc, I. Prebil, Low-cycle fatigue properties of steel 42CrMo4, *Mat. Sci. Eng. A*, 345 (**2003**), 278–285

[14] R. Kunc, Low cycle carrying capacity for bearing raceway with hardened rolling surface, Ph.D. Thesis, University of Ljubljana, 2002

[15] R. Kunc, I. Prebil, Numerical determination of carrying capacity of large rolling bearings. *J. Mater. Process. Technol.*, 155/156 (**2004**), 1696–1703

ANISOTROPIC HARDENING OF MATERIALS BY NON-SHEARABLE PARTICLES

UTRDITEV ANIZOTROPNIH MATERIALOV Z DELCI

[1]Napo Bonfoh, [2]Sonnou Tiem, [1]Paul Lipinski

[1]Laboratoire de Fiabilité Mécanique (L.F.M.), Ecole Nationale d'Ingénieurs de Metz (E.N.I.M.), Ile du Saulcy, F 57045 Metz Cedex 01, France
[2]Ecole Nationale Supérieure d'Ingénieurs (E.N.S.I.), Université de Lomé, B.P. 1515 Lomé, Togo
bonfoh@enim.fr; sonnou.tiem@togotel.net.tg; lipinski@enim.fr

A new description of the hardening of polycrystalline materials is proposed. This hardening is mainly induced by non-shearable particles. Anisotropic and kinematic hardening of this kind of material has been mentioned in a previous paper (Bonfoh et al., 2003). In contrast to this initial investigation, the proposed modified formulation introduces a non-linear hardening for the single crystal without particles and better renders the material behaviour at finite deformations. The micromechanical modelling is based on a two-level homogenization approach: a micro-mesoscopic transition is firstly performed to derive the equivalent behaviour of a single crystal containing a volume fraction of intra-crystalline particles. Then, a second transition to the macroscopic scale leads to the elastic-plastic behaviour of the polycrystalline material. The numerical results of the model are analysed in terms of the internal stress developed during plastic loading. The material behaviour, when subjected to a multiaxial loading, is also studied through the concept of the yield surface. Some other aspects, such as the influence of particles size, shape and volume fraction, are also investigated.

Key words: crystal plasticity, inhomogeneous material, residual stress, yield surface, kinematic hardening

Predložen je nov opis utrditve polikristalnih materialov. To utrditev povzročajo nestrižni delci. V prejšnjem delu je bila opisana anizotropična in kinematična utrditev materiala te vrste (Bonfoh in dr., 2003). Nasprotno od te začetne raziskave predložena modificirana formulacija uvaja nelinearno mikromehansko modeliranje za nanokristal brez delcev in bolje opisuje vedenje materiala pri končni deformaciji. Mikromehansko modeliranje temelji na približku dvostopenjske homogenizacije: mikro-mezoskopska tranzicija je uporabljena za opis ekvivalentnega vedenja monokristala, ki vsebuje neki prostorninski delež intrakristalnih delcev, nato pa tranzicija na makroskopsko merilo vodi v elasto- plastično vedenje polikristalnega materiala. Numerični rezultati modela so analizirani s stališča notranjih napetosti, ki nastanejo pri plastični obremenitvi. Vedenje materiala pri večosni obremenitvi je analizirano s stališča plastičnega popuščanja površine. Analizirani so tudi drugi vidiki, npr. vpliv velikosti oblike in prostorninskega deleža delcev.

Ključne besede: plastičnost kristala, nehomogen material, zaostale napetosti, plastično popuščanje površine, kinematična utrditev

1 INTRODUCTION

Most polycrystalline materials exhibit, at the microscopic level, some heterogeneities, such as foreign atoms or particles. These heterogeneities, which may appear in the form of a solid solution or second-phase particles, may be located either between the crystals or inside the single crystals of the polycrystalline materials. In the present study, only the latter heterogeneities are considered. These intra-crystalline particles, such as precipitates, interact with moving dislocations during the material's plastic flow and lead to a modification of the single-crystal hardening.

Some papers have been devoted to a description of the influence of intra-granular heterogeneities on the behaviour of polycrystalline materials: Schmitt et al (1996), Bochet et al (2001), Barbe et al. (2001) and Han et al. (2004). Recently, Reza et al (in press) has proposed a description of crystalline materials containing non-interacting elastic particles. Performed within a small strain formulation and confined to uniform elasticity, the authors propose a calculation of the additional work of deformation (strain energy) arising from plastic strain-field incompatibilities between the elastic-plastic matrix and the elastic particles.

In this work, a micromechanical description of a single crystal containing particles is developed through a micro-meso transition. First, a modified Schmidt's law and a new hardening matrix, taking into account the usual dislocation-dislocation interactions and also the interactions between dislocations and particles, are proposed. Next, a meso-macro transition using the self-consistent method developed by Lipinski et al. (1993, 1998) is applied to deduce the global response of the polycrystalline material. A comparison between the classical self-consistent predictions and the new approach is made. Special attention has been focused on the prediction of the yield surfaces and the residual stresses.

2 DESCRIPTION OF THE SINGLE CRYSTAL WITH PARTICLES

In this paper, single crystals are assumed to contain a certain volume fraction of ellipsoidal particles. Moreover, at the microscopic level, the single crystal is

considered as a two-phase material: the elastic-plastic crystalline matrix with elastic particles. The plastic straining of the crystal results from the movements of dislocations on geometrically well-defined slip planes. The classical theory of single-crystal plasticity is adopted and Schmidt's law is valid.

At the crystalline level, the presence of non-shearable particles results in some incompatibilities of the strain field between the crystalline matrix and the particles. These incompatibilities are mainly due to the anisotropy of elastic behaviour and the heterogeneity of plastic straining between the matrix and the particles. The stress rate inside the crystalline matrix is then given by:

$$\dot{\sigma}^{m} = \dot{\sigma}^{1} + \tilde{P}:\dot{\varepsilon}^{m} \tag{1}$$

The last term $\tilde{P}:\dot{\varepsilon}^{m}$, represents internal stresses arising from these incompatibilities, where the fourth-rank tensor $\tilde{P}$ is the polarisation tensor describing the evident interactions between the two phases evolving inside the heterogeneous grain. The expression of this tensor $\tilde{P}$ can be derived using classical models of the interactions problems of heterogeneous materials (Kröner, Mori-Tanaka, Self-consistent, etc.). In this study, the last of these is used, and this leads to:

$$\tilde{P} = f(\tilde{I} - \tilde{b}^{3}):\tilde{l}^{1}(\tilde{I} - f\tilde{a}^{3})^{-1} \tag{2}$$

where $\tilde{a}^{3}$ and $\tilde{b}^{3}$ are, respectively, the strain- and stress-rate localisation tensors inside the particles, $\tilde{l}^{1}$ is the tangent elastic-plastic moduli of the equivalent single crystal with particles.

Moreover, assuming the following relationship for the hardening of the single crystal without particles:

$$\tau_{cr}^{g} = \sum_{h=1}^{N} H^{gh}\dot{\gamma}^{h} \tag{3}$$

It is also possible to derive a kind of Schmidt law for the equivalent heterogeneous grain:

$$R^{g}:\left[(1-f)\tilde{I} + \tilde{P}:\tilde{s}^{m}(\tilde{I} - f\tilde{b}^{3})\right]:\dot{\sigma}^{1} =$$
$$= \sum_{h=1}^{N}(H^{gh} - R^{g}:\tilde{P}:R^{h}):(1-f)\dot{\gamma}^{h} \tag{4}$$

The first term appears as the resolved shear-stress rate for the equivalent grain I subjected to the $\dot{\sigma}^{I}$ stress rate, where the second one reveals a new form of hardening matrix:

$$\aleph^{gh} = H^{gh} - R^{g}:\tilde{P}:R^{h} \tag{5}$$

taking into account the initial dislocation-dislocation interactions through the matrix H^{gh} but also the interactions between the particles and the dislocations during their movements ($R^{g}:\tilde{P}:R^{h}$).

The description of the equivalent behaviour of the single crystal with particles is therefore completed by the expression of its tangent elastic-plastic properties:

$$\tilde{l}^{1} = \tilde{C}^{1} - \sum_{g=1}^{N}\sum_{h=1}^{N}\tilde{C}^{1}:R^{g}K^{gh}R^{h}:\tilde{U}:\tilde{C}^{1} \tag{6}$$

$$\tilde{U} = (1-f)\tilde{I} + \tilde{P}:\tilde{s}^{m}:(\tilde{I} - f\tilde{b}^{3}) \quad \text{and}$$
$$K^{gh} = (\aleph^{gh} + R^{g}:\tilde{U}:\tilde{C}^{1}:R^{h})^{-1} \tag{7}$$

The superscripts m, 3 and I are, respectively, related to the matrix (single crystal without particle), particles and the considered grain I.

After this first transition from local microscopic properties to the mesoscopic level, leading to the grain behaviour, a second transition, to the macroscopic level, is then performed to derive the equivalent properties of the polycrystalline material consisting of a large number of single crystals with particles.

3 NUMERICAL SIMULATIONS

The proposed model is applied to the simulation of the material's behaviour. The selected material is a SiC particulate-reinforced 5456 aluminium alloy matrix composite:

- Matrix material (aluminium): Young's modulus E_m = 73 GPa, Poisson's ratio ν_m = 0.33, and initial uniaxial yield stress σ_y = 230 MPa.
- Elastic properties of SiC particles: Young's modulus E_p = 485 GPa and Poisson's ratio ν_p = 0.2.

3.1 Material behaviour under monotonous loading

The selected material is subjected to a uniaxial tension in direction 1, and its macroscopic response in terms of stress–strain is depicted in **Figure 1**.

The plotted curves exhibit an evident hardening of the macroscopic behaviour with the volume fraction of particles, since the particles considered here are harder than the crystalline matrix. Moreover, this hardening is characterized by an increasing of the equivalent elastic threshold and a non-linear evolution in its elastic-plastic part. Since the initial hardening of the single crystal is assumed linear, this non-linear aspect results from the original amendments introduced in the proposed hardening model.
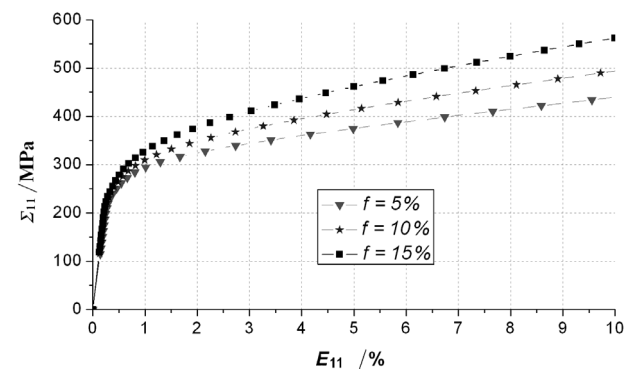
Figure 1: Macroscopic response for different volume fractions of particles

Slika 1: Makroskopski odgovor za različen volumenski delež delcev

In the present investigation, particles are non-shearable and during the plastic flow, dislocations bypass these obstacles with the Orowan-looping mechanism.

The initial critical shear stress on slip systems is influenced by particle interactions at the beginning of the plastic flow.
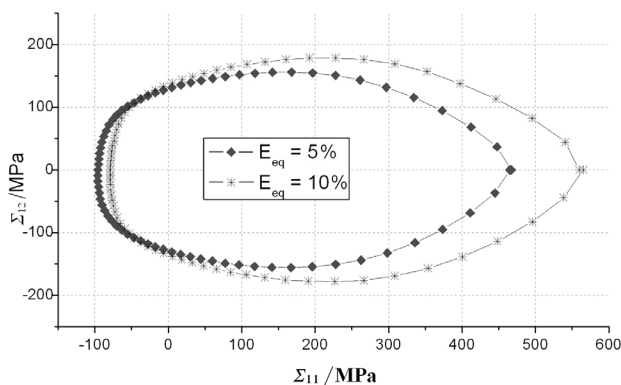
3.2 Yield surface

The material behaviour during multiaxial and non-proportional loads is analysed through the concept of a yield surface depicted in a stress plane. The yield surfaces proposed in this study are determined for a plastic offset of $E_{eq}^{p} = \sqrt{2/3 E_{ij}^{p} E_{ij}^{p}} = 0.2$ %. The results in **Figure 2** correspond to the same material identified in the previous paragraph, and represent the macroscopic yield surface after two amounts of macroscopic equivalent strain ($E_{eq} = 5$ %, $E_{eq} = 10$ %) of a tensile pre-straining in direction 1.
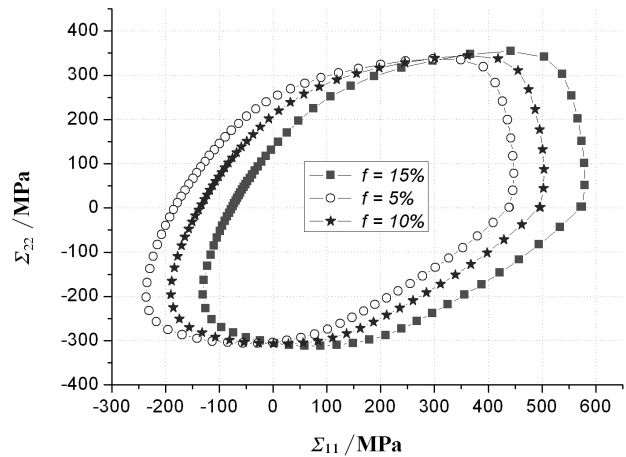
These yield surfaces reveal:

- A vertex in the pre-straining direction, due to great inter and intra-granular residual stress being developed. These back stresses arising from incompatibilities of strain fields pointed out previously, increase the yield stress in this pre-loading direction.
- A flattening of the yield surface in the opposite direction to the pre-straining is also observed. This relative softening results from the decrease of the yield stress due to superimposed back stresses in this opposite direction.
- A hardening in directions transverse to the pre-loading is also visible.

Whatever the amount of pre-straining, the obtained equivalent behaviour exhibits a mixed anisotropic and kinematic hardening due to the intra-crystalline particles. A translation in the pre-straining direction combined with a non-homogeneous expansion of the yield surfaces is observed in **Figure 3**.
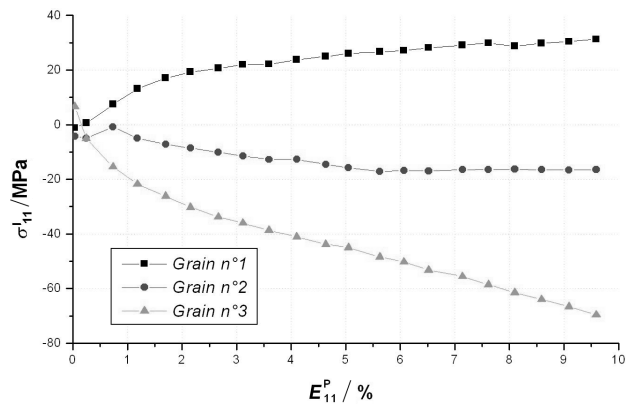

Figure 3: Material yield surfaces after a tensile pre-straining (in direction 1, $E_{eq} = 10$ %)
Slika 3: Površine plastičnega popuščanja materiala po natezni predobremenitvi (v smeri 1, $E_{eq} = 10$ %)

Figure 4: Residual stress inside particle after a tensile pre-straining (in direction 1)
Slika 4: Zaostale napetosti v notranjosti delca po natezni predobremenitvi (v smeri 1)

The presence of intra-crystalline-heterogeneities-induced internal stresses relates to the evident interactions between the latter and the dislocations during their movement. These internal stresses are developed both in the matrix and the particle, where a strong polarization is observed. After a pre-loading, leading to a significant permanent strain, followed by an unloading, there remains internal stresses called residual stresses. **Figure 4** depicts these residual stresses, developed inside particles for three selected grains of the polycrystalline material. Due to the elastic properties of the selected particles, these residual stresses seem to be relatively important for the macroscopic stress level. In contrast to previous investigation, their evolution is non-linear, because of the introduced new hardening matrix and differs from grain to grain.

Figure 2. Macroscopic yield surfaces after a tensile pre-straining (in direction 1)
Slika 2: Makroskopsko plastično popuščanje površine po natezni predobremenitvi (v smeri 1)

4 CONCLUSION

The paper proposes a new formulation for the hardening of polycrystalline materials due to intra-crystalline heterogeneities such as precipitates. The suggested model takes into account internal stresses arising from the incompatibilities of the strain field between the crystalline elastic-plastic matrix and the purely elastic particles.

The observed hardening has been elucidated with numerical simulations of the behaviour response under monotonous, uni- and multi-axial loadings. The results, in terms of the yield surfaces and the internal stresses evolution with the volume fraction of the particle and also with the amplitude of specific pre-straining, are provided.

These internal stresses, characterised by a strong polarisation in the particles, leads to important interfacial stresses and the subsequent damage initiation by the particle's interface debonding. For this specific problem, a combined stress and energetic criterion is introduced, to take into account the particles' size effect, pointed out for the damage initiation in such materials.

5 REFERENCES

[1] Ashby, M. F., The deformation of plastically non-homogeneous materials. Phil. Mag. 21 (**1970**), 399–424

[2] Berveiller M, Zaoui A., An extension of the self-consistent scheme to plastically-flowing polycrystals. J. Mech. Phys. Solids. 26 (**1984**), 325–344

[3] Barbe F., Decker L., Jeulin D., Cailletaud G., Intergranular and intragranular behavior of polycrystalline aggregates. Part 1: F. E. model. Int. J. Plasticity 17 (**2001**), 513–536

[4] Barbe F., Forest S., Cailletaud G., Intergranular and intragranular behavior of polycrystalline aggregates. Part2: Results. Int. J. Plasticity 17 (**2001**), 537–563

[5] Bochet, L., Delobelle, P., Robinet, P., Feaugas, X., Mechanical and microstructural investigations of an austenitic stainless steel under non-proportional loadings in tension-torsion-internal and external pressure. Int. J. Plasticity 17 (**2001**), 1491–1530

[6] Bonfoh N., Modélisation micromécanique de l'écrouissage des matériaux polycristallins contenant des hétérogénéités intra-granulaires. Introduction à l'endommagement ductile. PhD thesis, Université de Metz, 2001

[7] Bonfoh N., Lipinski P., Carmasol A., Modeling of intra-crystalline hardening of materials with particles. Int. J. Plasticity,19 (**2003**), 1167–1193

[8] Bonfoh N., Lipinski P., Carmasol A., Tiem S., Micromechanical modeling of ductile damage of polycrystalline materials with heterogeneous particles. Int. J. Plasticity, 20 (**2003**), 85–106

[9] Han, C. S, Wagoner, R. H., Barlat, F., On precipitate induced hardening in crystal plasticity: theory. Int. J. of Plasticity 20 (**2004**), 477–494

[10] Reza S. Yassar, Sinisa Dj. Mesarovic, David P. Field, Micro-mechanics of hardening of elastic-plastic crystals with elastic inclusions. I-Dilute concentration (submitted) Int. J. Plast.

[11] Schmitt C., Lipinski P., Berveiller M., 1997. Micromechanical Modelling of the elastoplastic behavior of polycrystals containing precipitates-Application to hypo- and hyper-eutectoid steels. Int. J. Plast. 13 (**1997**) 3, 183–199

ANALYSIS OF THE BORONIZED LAYER ON K 190 PM TOOL STEEL

ANALIZA BORONIZIRANE PLASTI V ORODNEM JEKLU K 190 PM, IZDELANEM PO POSTOPKU METALURGIJE PRAHU

Mária Hudáková, Martin Kusý, Viktória Sedlická, Peter Grgač

Department of Materials Engineering, Faculty of Materials Science and Technology, Slovak University of Technology, J. Bottu 24, 917 24 Trnava, Slovakia
maria_hudakova@stuba.sk

This work deals with the characterization of the phases in boronized layers formed for particular processing parameters on tool steel of the ledeburite type. The high-alloyed tool steel K190 PM prepared by powder metallurgy was used as a substrate. X-ray diffraction (XRD) measurements were carried out at different depths of boronized layers, as well as of transient layers, using a Philips PW1710 diffractometer. The analysis revealed that the surface consisted of FeB (MeB) and an unidentified crystalline phase (or phases), which amount decreases with increasing distance from the surface. Also, a gradual increase in the amount of Fe_2B (Me_2B) at the expense of MeB was observed with increasing distance from the surface. The layer neighboring the substrate consists mainly of Me_2B and CrB. The transition layer between the borides and the base material was found to contain the $Me_{23}(C,B)_6$ phase.

Key words: tool steel, boronized, layer, constitutive phases, microhardness

Predstavljena je karakterizacija faz v boronizirani plasti, pripravljeni na ledeburitnem orodnem jeklu. Kot podlaga je uporabljeno jeklo K 190 PM, pripravljeno po postopku metalurgije prahu. Difrakcija rentgenskih žarkov je bila izvršena pri različnih globinah boronizirane in prehodne plasti z difraktometrom Philips PW 1710. Analiza je pokazala na površini fazo FeB (MeB) in neidentificirano kristalno fazo (ali faze), katerih vsebnost se zmanjšuje z razdaljo od površine. Ugotovljena je tudi postopna rast količine faze Fe_2B (Me_2B) na račun faze MeB z oddaljevanjem od površine. Plast na meji s podlago je iz Me_2B in CrB. V prehodni plasti med boridi in osnovnim materialom smo našli faze $Me_{23}(C,B)_6$.

Ključne besede: orodno jeklo, boronizirana plast, sestavne faze, mikrotrdota

1 INTRODUCTION

In addition to the popular techniques of carburizing and nitriding, boronizing also plays an important, though less common, role in thermo-chemical treatments. Boronizing usually leads to the formation of a very hard and wear-resistant layer on the surface of the material. Due to the diffusion of the boron into the surface of the carbon steel, iron borides with very high hardnesses are formed. The boronized layers exhibit a higher hardness than the layers prepared with carburizing or nitriding. Generally, low-carbon and low-alloyed steels are boronized. This process can also be applied to austenite steels, non-ferrous alloys (nickel or cobalt), heat-resistant metals such as Ti and Ta and also to sintered carbides, such as WC-Co, with the aim of improving their wear resistance [1,2]. Boronizing is currently also used for a number of applications where no surface treatment has been used so far. It is applied to various forming tools, components working in an abrasive environment, dies for the injection casting of non-ferrous alloys and others. Furthermore, it is suitable for preparing functional layers with an extended lifetime of the substrate material due to the increased hardness of the surface. During the boronizing of plain steels, FeB or Fe_2B is formed in the surface layers. The thickness of the boride layers typically varies in the range from 20 to 300

μm [3,4]. The aim of this paper is to present a detailed XRD characterization of the boronized layer formed on the surface of K 190 PM high-alloyed tool steel.

2 EXPERIMENTAL

The boronized layer investigated was formed on K 190 PM tool steel prepared by powder metallurgy. The chemical composition of the steel is shown in **Table 1**.

Table 1: Chemical composition of K 190 ISOMATRIX PM steel
Tabela 1: Kemijska sestava jekla K 190 ISOMATRIX PM

Chemical element	Fe	C	Si	Mn	P	S	Cr	V	Mo
Content $w/\%$	balance	2.29	0.5	0.32	0.026	0.019	12.3	4.06	1.06

The steel was delivered as a rod with a diameter of 10 mm. For the purpose of the boronizing experiment, the rod was cut into 10-mm-long pieces. The pieces were cleaned and degreased and boronized at at 1000 °C for 8 h in a (80 × 85 × 125) mm hermetic container filled with a *DURBORID* powder mixture. After boronizing the samples were cooled to room temperature in containers in the open air. The microstructure of the boronized K 190 PM tool-steel layer consisted of a boride and a transient layer. The microhardnesses of the boride layer,

the transient layer, and the substrate were measured with a Hannemann indenter fitted to a Zeiss Neophot 21 light microscope.

The XRD patterns of the boride layer, the transient layer and the substrate were recorded with a Philips PW 1710 diffractometer using Fe-filtered CoK_{α} radiation. The experimental device was equipped with a secondary graphite monochromator and a pulse-height proportional detector. Data were recorded in the range 20–144° (2θ) using a constant step of 0.05° and a 10 s exposure time and samples rotating. Qualitative and quantitative analyses of the phases were also carried out using X-ray diffraction on the as-delivered substrate of soft-annealed K 190 PM steel.

Exploiting the natural penetration depth of the X-ray radiation, the analysis was performed in consecutive steps. First, the as-prepared boronized substrate without any mechanical cleaning was examined using XRD and microhardness measurements. Next, a predetermined volume of the surface layer was removed with grinding with APEX diamond discs. The new surface was then examined using the same experimental tools. The series contained a total of 10 XRD patterns, taken from the as-prepared surface and the surfaces at the depth of (2, 7, 20, 30, 40, 50, 60, 70, 80) μm. It should be emphasized that the information extracted from a single diffraction pattern taken from a boride layer represents the volume corresponding to the penetration depth of X-rays. Therefore, it cannot be considered as a characterization of the surface but rather of a layer of a certain thickness located at various depths.

The identification of the peaks in the XRD patterns was based on a comparison of the calculated hkl and the d_{hkl} list of relevant phases determined from the chemical composition of the substrate, further revised with data on the phase identification in the boride layers [1-5]. For the quantitative treatment of the XRD data the Powder Cell 2.4 computer program and, in special cases, the MAUD program based on a Rietveld algorithm [6-8] were used. All the crystallographic data used for the calculation of the theoretical diffraction patterns were taken from Pearson's handbook [9].

3 RESULTS AND DISCUSSION

The microstructure of the soft-annealed substrate of K 190 PM is shown in Figure 1. It consists of a uniform distribution of small spheroidized M_7C_3 and MC carbides in the ferrite matrix, which is characteristic for the soft annealed K 190 PM tool steel. The results of the quantitative phase analysis of the substrate determined from the XRD (Figure 1) by the Rietveld method using the Maud computer program are shown in the table in **Figure 1**.

Figure 2 shows the XRD data collected at different depths of the boride and transient layers. The XRD pattern taken from the as-prepared surface and from 2
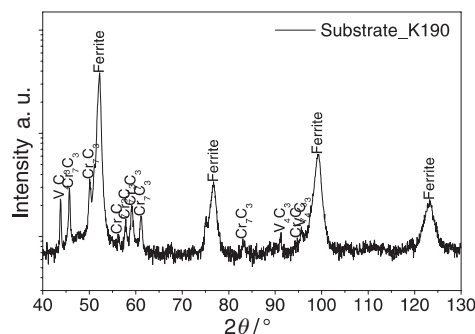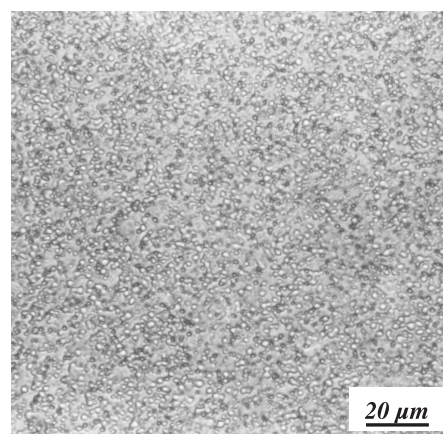
Phase	Ferrite	V$_4$C$_3$	Cr$_7$C$_3$
Quantity φ / %	72.1 ± 1.4	5.6 ± 0.1	22.3 ± 0.4

Figure 1: Microstructure and XRD pattern of the soft-annealed K 190 PM steel. A table summarizing the amounts of the different phases is included

Slika 1: Mikrostruktura in XRD-posnetek mehko žarjenega jekla s tabelo z vsebnostjo različnih faz

μm and 7 μm into the boronized layer consist of the dominant FeB (MeB), the minor Fe$_2$B (Me$_2$B), CrB, and an unidentified phase (or phases).

The diffraction peaks attributed to the unidentified phase (or phases) did not appear in the diffraction pattern taken from the surface located at a depth of 20 μm. The intensity of the reflections attributed to the Me$_2$B phase increased slightly between the 7-μm and 20-μm scan.

The observed trend of increasing intensity of the Me$_2$B phase was confirmed with a series of XRD scans taken from depths of 30 μm and 40 μm. It can be concluded from the next layer in the series, taken from a depth of 50 μm, that the MeB phase becomes a minor phase. It is also possible to observe two strong reflections of the Me$_2$B phase with increasing intensity. Moreover, the reflection observed at approximately 52° (2θ) suggests an increasing diffraction intensity of the ferrite matrix.

Both the MeB and the Me$_2$B observed in the depth ranges from 0 μm to 60 μm were influenced by epitaxial growth of the (020) and (002) planes, respectively.

When the material from the boronized layer is removed down to 70 μm or 80 μm the XRD patterns change significantly. It was found that the layer down
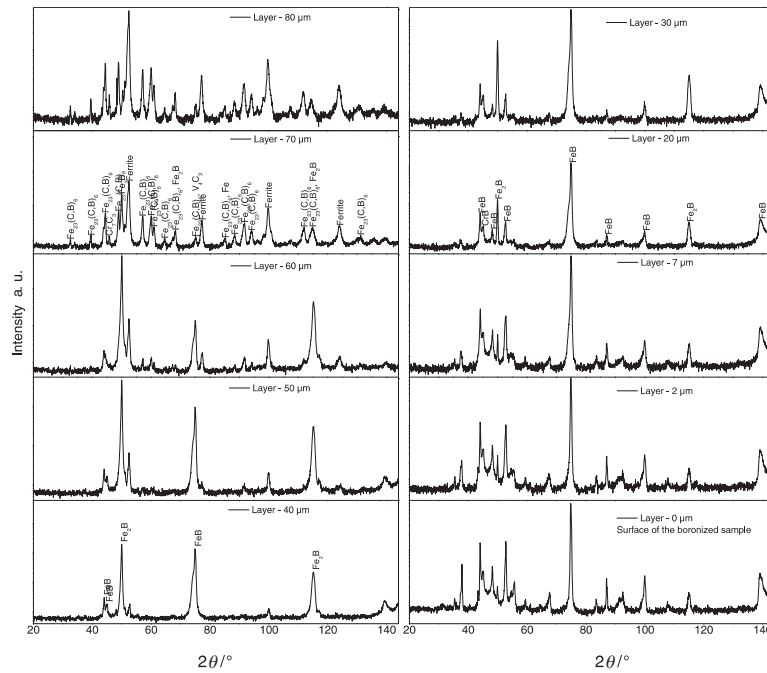
Figure 2: XRD patterns taken from a series of depths in the boronized layer formed on K190 PM tool steel
Slika 2: XRD-posnetki pri različnih globinah boronizirane plasti na jeklu K 190 PM

below 70 μm contains complex iron-chromium carbo-boride, with a crystal structure corresponding to $Me_{23}(C,B)_6$, and ferrite. Neither MeB nor Me_2B were identified in this depth range. It is, therefore, suggested that the patterns taken from depths of 70 μm and 80 μm are already located in the transient zone between the boride layer and the substrate. The presence of this phase agrees well with earlier publications, where Cr was considered to be an element less soluble in the boride layer. As a result of this behavior, Cr is enriched in the transient zone ahead of the boride layer and forms the complex Cr-based carbide $Me_{23}(C,B)_6$ or carbo-borides, where carbon is partially replaced with boron [5].

A simplified representation of the phase composition in the boride and the transient layers is shown in **Figure 3a** in the form of a color map of dominant phases as a function of layer depth. The map shows that Fe_2B (Me$_2$B) and FeB (MeB) are present in both the boride and the transition layers after 8 hours of boronizing at 1000 °C.

Figure 3b shows the quantity of FeB (MeB) and Fe_2B (Me$_2$B) determined from XRD patterns and the variation of the microhardness as a function of the depth of the layer. The quantity of MeB and Me$_2$B was determined neglecting other phases (the unidentified phase (or phases), CrB and $Me_{23}(C,B)_6$). The quantitative results were obtained from the Rietveld algorithm implemented in Powder Cell 2.4 [6]. In this graph, the microhardness profile across the analyzed depth profile is also shown. The color map (**Figure 3a**), in combination with the quantity of phases and the microhardness
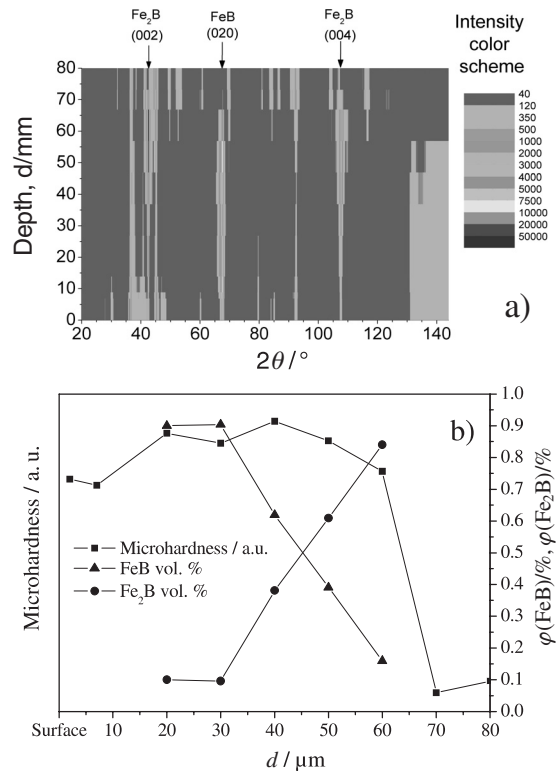
Figure 3: Color map showing the occurrence of the identified phases as a function of the layer depth determined from XRD (**3a**) and the quantities of FeB (MeB) and Fe_2B (Me$_2$B) determined from the XRD experiment and the microhardness profile plotted as function of the depth of the layer (**3b**).
Slika 3: Barvni prikaz prisotnosti identificiranih faz v odvisnosti od globine plasti, določen z XRD-posnetkom (**3a**), vsebnost FeB (MeB) in Fe$_2$B (Me$_2$B) določene iz teh posnetkov in mikrotrdota v odvisnosti od globine plasti (**3b**)

profile shown in **Figure 3b**, is proposed as an effective tool for designers and producers.

4 CONCLUSIONS

The paper presents an estimate of the quantities of MeB and Me_2B at various depths in the boronized layer. The quantitative evaluation was performed, neglecting other phases (an unidentified phase (or phases) or CrB and $Me_{23}(C,B)_6$) present in the boronized layer. It was found that the uppermost layers, down to the depth of 20 μm, consist of MeB and some unidentified phases. The amount of unidentified phase (or phases) decreases with the increasing depth below 7 μm and this phase is not found at the depth of above 20 μm. Most of the MeB was found in the layers from 20 μm to 40 μm. MeB was not found in the layers from 70 μm to 80 μm. The majority of the Me_2B was found in the range from 50 μm to 60 μm. A minor amount of this phase was found in other layers over the entire thickness of the boronized layer. A strong epitaxy into the (020) and (002) planes was observed for the growth of the MeB and Me_2B, respectively. The CrB phase was identified in small quantities from XRD patterns in the range from 0 μm to 50 μm from the surface. Diffraction patterns from depths of 70 μm to 80 μm revealed the presence of $Me_{23}(C,B)_6$, which identifies this region as the transient layer. The highest microhardness of the boronized layer was observed in the range 20 μm to 50 μm from the surface.

In the range from 0 μm to 20 μm the measured microhardness was found lower down, probably due to the influence of the unidentified phase (or phases).

5 REFERENCES

[1] Dufek, V., Schejbal, T., Brožek, V.: Strojírenská výroba, 34 (**1986**) 3, 197–200

[2] Bhushan, B., Gupta, B. K.: Handbook of Tribology, McGraw – Hill, Inc., New York, 1991

[3] Kroulík, M.: Strojírenská výroba, ČVUT, Praha, 1991, 8–11

[4] Grafen, W., Edenhofer, B.: New developments in thermo-chemical diffusion processes, Surface & Coatings Technology 200 (**2005**), 1830–1836

[5] M. A. Bejar, E. Moreno, Abrasive wear resistance of boronized carbon and low-alloy steels, Journal of Materials Processing Technology 173 (**2006**), 352–358

[6] Kraus, W., Nolze, G.: PowderCell for Windows, Version 2.4, Federal Institute for Materials Research and Testing, 2000

[7] Lutterotti, L., Matthies, S., Wenk, H.-R.: MAUD: a friendly Java program for material analysis using diffraction. IUCr: Newsletter of the CPD, 21 (**1999**), 14–15

[8] Young, R. A.: The Rietveld Method, Oxford University Press, 1995

[9] Villar, P., Calvert, L. D.: Pearson's Handbook of Crystallographic Data for Intermetallic Phases, Vol. 1, American Society for Metals, 1989

A CO-PRECIPITATION PROCEDURE FOR THE SYNTHESIS OF LSM MATERIAL

SOOBARJANJE LSM ZA PRIPRAVO KATODNIH MATERIALOV ZA GORIVNE CELICE

Marjan Marinšek, Klementina Zupan, Tanja Razpotnik, Jadran Maček

Faculty of Chemistry and Chemical Technology, University of Ljubljana, Aškerčeva 5, 1000 Ljubljana, Slovenia
marjan.marinsek@fkkt.uni-lj.si

Lanthanum manganite substituted with strontium is a strong candidate for use as a mixed conductor at the cathode site in solid-oxide fuel-cell systems. In the present work a co-precipitation method for the preparation of LSM is described and some material properties are reported. Since the co-precipitation involved calcination at 1000 °C and subsequent sintering, the crystalline phase development and the material homogeneity were followed by X-ray powder diffraction. It was found that no secondary crystalline phases were present in the system when the samples were thermally treated up to 1200 °C. The sintering behaviour of the calcined powders and their density evolution are also reported. Relatively dense bodies were prepared after thermal treatment at 1200 °C for 2 hours. The electrical characteristics of the material were determined from screen-printed LSM sintered layers. The electrical conductivity of the screen-printed layers increased with the sintering temperature due to an additional densification effect. Porous LSM bodies were prepared by methyl cellulose admixing as a pore-former.

Key words: co-precipitation, lanthanum strontium manganite, microstructure, electrical conductivity

Najpogosteje uporabljan katodni material v visokotemperaturni izvedbi gorivnih celic (SOFC) je lantanov manganit, dopiran s stroncijem (LSM). LSM s sestavo La$_{0,85}$Sr$_{0,15}$MnO$_{3-\delta}$ smo pripravli z novo metodo soobarjanja iz raztopine karbonatov. Oborino smo po filtraciji in spiranju sušili pri 110 °C in nato kalcinirali pri 1000 °C. Po kalcinaciji pri različnih temperaturah in po sintranju smo prahove analizirali z rentgensko praškovno analizo. Materiali so po sintranju vsebovali le perovskitno kristalno obliko lantanovega manganita. Parametre sintranja prahov LSM po kalcinaciji pri 1000 °C smo določili s segrevalnim mikroskopom. Vzorce LSM z dodatkom tvorca por in brez njega smo po sintranju analizirali z elektronsko mikroskopijo. Električne karakteristike tiskanih plasti LSM smo določili s štiritočkovno metodo. Specifična električna prevodnost pripravljenih plasti LSM je primerljiva z literaturnimi podatki za materiale LSM, ki so bili pripravljeni po kalcinacijskem postopku.

Ključne besede: koprecipitacija, lantanov stroncijev manganit, katoda, mikrostruktura, električna prevodnost

1 INTRODUCTION

Lanthanum strontium manganite (LSM) is known as a potential cathode material for solid-oxide fuel cells (SOFCs) based on a stabilized zirconia electrolyte [1]. In the present generation of SOFCs a nominal composition of La$_{1-x}$Sr$_x$MnO$_3$ ($x < 0.2$) is normally used. The use of LSM-based cathode materials depends not only on their chemical, structural and thermodynamic characteristics but also on their final microstructure, grain size, pore size and pore-size distribution [2-4]. The porosity and pore-size distribution, in particular, play a significant role because of the double role of the LSM in the SOFC system, i.e., the LSM has to be an effective electro-catalyst and at the same time has to be permeable to cathode gases.

Another aspect when LSM is used as the cathode material is its homogeneity and the possible interaction with the zirconia-based electrolyte. One potential interaction between the LSM cathode layer and the zirconia-based electrolyte in the SOFC system is diffusion (at the phase boundary) of the Y$_2$O$_3$ from the YSZ into the LSM phase. This diffusion leads to the formation of tetragonal and/or monoclinic ZrO$_2$. Such a ZrO$_2$ crystal-structure transformation is accompanied by a volume change and, as a result, possible crack formation (more intense when the SOFC system is repeatedly heated up and cooled down) [5]. Another problem arises if products with a high electrical resistivity at the cathode/electrolyte phase boundary, like La$_2$Zr$_2$O$_7$, are formed. The La$_2$Zr$_2$O$_7$ phase is normally found in systems based on LaMnO$_{3+d}$/YSZ after a prolonged treatment at high temperatures [6]. To suppress the La$_2$Zr$_2$O$_7$ formation, La-manganite is doped with Sr in relatively low concentrations

(La$_{1-x}$Sr$_x$MnO$_3$; $x < 0.3$). Larger additions of Sr also mean a higher risk of new low-conducting SrZrO$_3$ phase formation. The reactions between LSM and YSZ are more pronounced at higher temperatures, lower oxygen partial pressures and for prolonged reaction times.

The microstructure and homogeneity characteristics of LSM depend to a large extent on the processing conditions and are hard to control in the conventional ceramic synthesis process, which is based on the diffusion of the components in the solid state at high temperatures. For this reason alternative preparation routes for LSM synthesis based on wet chemical methods have been proposed. A characterization of perovskite powders for the cathode and oxygen

membranes prepared by different chemical routes was made by Sefir et al. [7], while the effect of the synthesis route on the catalytic activity of LSM was studied by Bell et al. [8]. The results of these studies implied that the carbonate co-precipitation synthesis route delivers a finer powder with more homogeneous composition and surface structure and is thus more suited for mixed conductor applications in SOFC systems. They both based the LSM preparation on the carbonate co-precipitation method, following the route described by Tanaka et al., where Na_2CO_3 was used as the precipitating agent [9]. Another co-precipitation-based LSM preparation was developed by Ghosh et al. [10] using ammonium carbonate as the precipitating agent.

In the present work we applied the carbonate co-precipitation route for batch LSM preparation. Sintering and microstructure-development studies were carried out for the calcined powder. Prepared LSM bodies were also characterised in terms of their electrical conductivity. Since a requirement of the cathodes for a SOFC is a porous body with almost 40 % open porosity, we also modified the cathode material by the addition of a former.

2 EXPERIMENTAL

In order to prepare stock solutions of 0.5-M lanthanum nitrate and strontium nitrate, lanthanum oxide (La_2O_3) and strontium carbonate ($SrCO_3$) were separately carefully dissolved in concentrated nitric acid, while manganous nitrate ($Mn(NO_3)_2 \cdot 4H_2O$) was dissolved in distilled water. Predetermined amounts of each solution were then mixed for $La_{0.85}Sr_{0.15}MnO_3$ preparation. The mixed solution was added drop-wise to a precipitating bath containing an aqueous solution of ammonium carbonate in which the amount of ammonium carbonate was in 50 % excess for complete precipitation of the mixed La-Mn-Sr-precursor. The pH of the precipitating bath was kept constant at 8.0 by small additions of aqueous ammonia. The temperature of the reaction mixture in the precipitating bath was adjusted to 65 °C and kept constant. The precipitation reaction took place in a CO_2 atmosphere to prevent any undesired oxidation of the manganese to MnO_2. The reaction time for the complete co-precipitation process was approximately 3 h.

The precipitate was easily filterable, and after filtration was washed several times with 0.125-M aqueous ammonium-carbonate solution. The washed precipitate was dried, first at room temperature under a CO_2 atmosphere for several hours, and afterwards, for 6 hours at 110 °C in air. Prior to calcination in a muffle furnace at 1000 °C for 1 hour, the dried powder was ground in an agate mortar. Calcined LSM powders were wet milled in isopropanol, pressed into tablets ($\Phi = 6$ mm, $h = 4$ mm, $p = 70$ MPa) and sintered at (1150, 1200 and 1250) °C for 1 h.

The carbonate co-precipitation route described above is also suitable for the preparation of larger quantities of mixed La-Sr-Mn-carbonate. The method is also very reliable and the final precipitate is easy to reproduce. To corroborate the above statement we prepared mixed La-SrMn carbonate in three different batches (S1, S2, and S3) and compared some of their properties. Typical quantities of initial precursors consumed in one cycle of the bath precipitation were 100 g of $(NH_4)_2CO_3$ dissolved in 2.5 L of H_2O, 854 mL of 0.5-M Mn-precursor solution, 363 mL of 0.5-M La precursor solution, and 128 mL of 0.5-M Sr precursor solution. Such a reaction mixture yielded approximately 100 g of final calcined LSM powder. Samples were characterized with the X-ray powder-diffraction technique using D4 ENDEAVOR apparatus. The shrinkage during sintering was measured by a LEITZ WETZLAR heating microscope.

LSM samples with the mass fraction of 10 % of pore former (methyl cellulose) were mixed in a ball mill for (3, 30 and 180) min, pressed into pellets and then sintered at 1200 °C for 1 h. After sintering the samples were polished and thermally etched and analyzed with an SEM (Zeiss FE SUPRA 35 VP). The quantitative analyses of the microstructures was performed using a Zeiss KS300 3.0 image-analysis system.

Samples for the electrical measurements were prepared by screen-printing LSM pastes on alumina substrates. Prior to printing the LSM powder was dispersed in an organic liquid phase in ratios from 40 % solid LSM powder and 60 % liquid phase, and then submitted to a homogenization procedure.

3 RESULTS AND DISCUSSION

The calcined powders (for XRD study purposes the calcination of the precursor carbonate-hydroxide powder was carried out in the temperature range 1000–1300 °C)
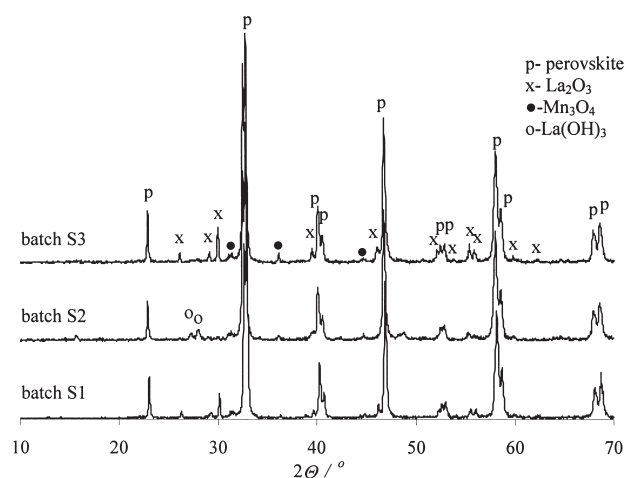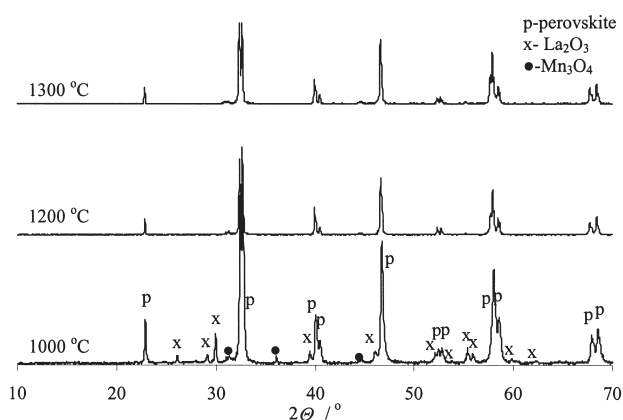

Figure 1: XRD patterns of the powder samples calcined at 1000 °C
Slika 1: Praškovni posnetki vzorcev, kalciniranih pri 1000 °C

were submitted to XRD examination. The XRD patterns of the powder samples prepared from the three different batch experiments calcined at 1000 °C are shown in **Figure 1**.

According to **Figure 1** perovskite LSM phase formation (LSM XRD peaks are denoted with the letter p) is practically complete; after calcination at 1000 °C the LSM perovskite phase is quite well crystallised. XRD analysis revealed only traces of the residual secondary phases Mn_3O_4 and La_2O_3 or $La(OH)_3$ resulting from the reaction of lanthanum oxide with moisture, forming lanthanum hydroxide (all denoted in **Figure 1**). The relatively small amount of secondary phases in the sample calcined up to 1000 °C makes the co-precipitation method favourable when compared to synthesis processes that are based on the diffusion of the components in the solid state (in this case the amount of secondary phases is normally greater). If the calcination temperature is increased (1200 °C or 1300 °C, **Figure 2**) the secondary phases are completely dissolved in the perovskite structure.

The shrinkage behaviour of the LSM powders prepared with other batch experiments and calcined at 1000 °C are shown in **Figure 3**. All the samples exhibit a normal thermal expansion in the temperature range below 1000 °C. This region of thermal expansion is followed by a single region of rapid sintering. The rate of rapid shrinkage varies slightly for each sample, which may be a consequence of some differences during the wet milling process. Above 1300 °C the powder shrinkage curves show a flattened region, this is due to completion of the rapid sintering stage and the initiation of the final sintering stage with closing of the entrapped porosity. The final shrinkage (25.8 ± 0.4) % of different LSM batches does not diverge substantially.

The shrinkage behaviour of LSM powders prepared with other batch experiments and calcined at 1000 °C are shown in **Figure 3**. All samples exhibit normal thermal
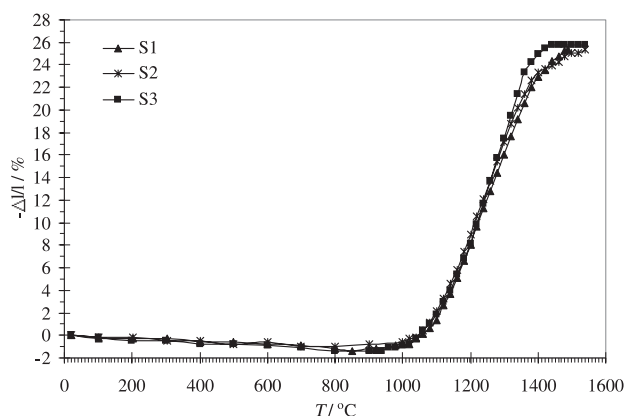
Figure 3: Typical shrinkage curves of LSM powders prepared in different batch experiments
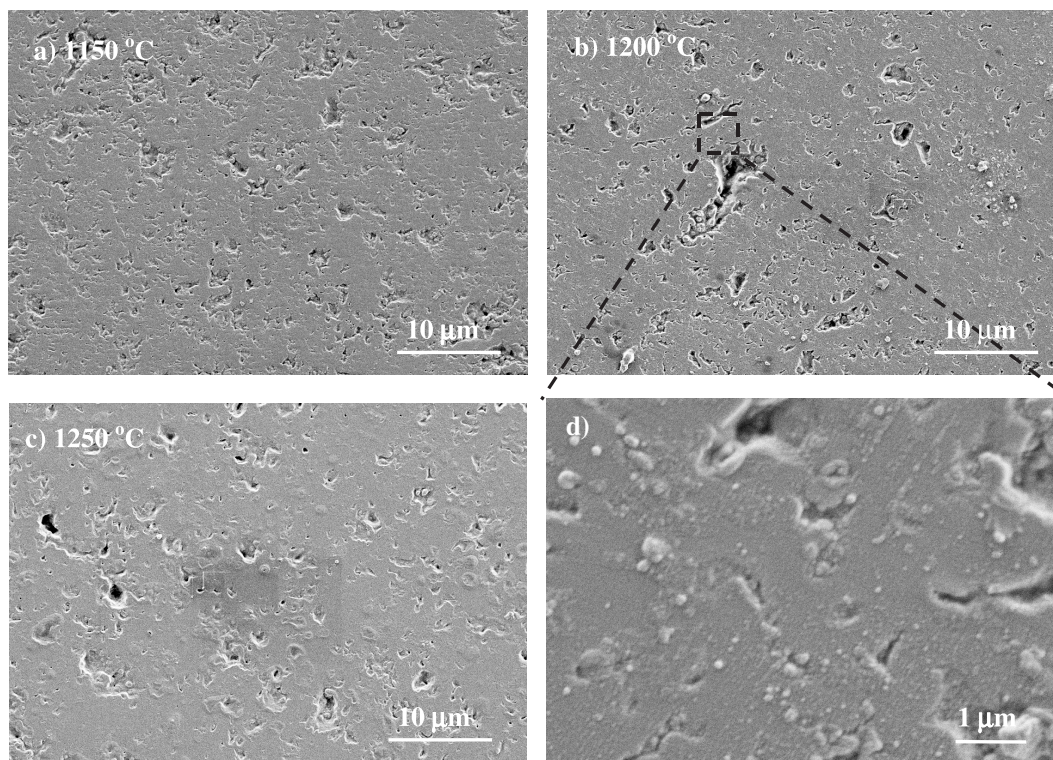**Slika 3:** Značilne krivulje sintranja vzorcev LSM za tri poskuse obarjanja

expansion in the temperature range below 1000 °C. This region of thermal expansion is followed by a single region of rapid sintering. The rate of rapid shrinkage varies slightly for each sample, which may be a consequence of some differences during the wet milling process. Above 1300 °C the powder shrinkage curves show a flattened region, this is due to completion of the rapid sintering stage and initiation of the final sintering stage with closing of the entrapped porosity. The final shrinkage (25.8 ± 0.4) % of different LSM batches does not diverge substantially.

Considering the results of the sintering curves, the sintering temperatures and sintered densities were calculated for all batch-prepared LSM materials. The sintering started at approximately 1050 °C. The sintering temperature and the sintered density varied from 1250 °C to 1280 °C with an average value calculated to be 1265 °C, and 5.61 g/cm^3 to 6.10 g/cm^3, with an average calculated value 5.84 g/cm^3, respectively. The shrinkage process finished at approximately at 1390 °C.

Scanning electron micrographs of an average LSM sample (batch S3) sintered at different sintering temperatures (1 hour of sintering) are presented in **Figure 4**. In general, with increasing sintering temperature the LSM microstructure becomes denser. However, the three microstructures presented (**Figure 4a–d**) do not differ significantly, implying that LSM can be successfully sintered, even at 1150 °C.

The above micrographs show a microstructure with denser regions as well as regions with some porosity in the micrometre range. If the dense regions are examined in greater detail (**Figure 5**), excellent particle-to-particle packing can be seen. These regions contain practically no porosity. Such a microstructure with completely dense regions separated by micrometer-range pores could be a consequence of insufficient powder homogenization prior to the sintering tests. Namely, any larger agglomerates left in the powder material after the wet-milling process would cause differences in the

Figure 2: XRD patterns of the powder S1 calcined at different temperatures
Slika 2: Praškovni posnetki vzorca S1, kalciniranega pri različnih temperaturah

Figure 4 (a–d): SEM micrograph of LSM material sintered at different temperatures
Slika 4 (a–d): Posnetki vzorcev LSM po sintranju pri različnih temperaturah

density through the sample. However, the fact that the LSM powder can be sintered at relatively low temperatures (less than 1200 °C, if the material is properly treated prior to sintering) is very important from the applicability point of view. If the material is used as a cathode in SOFC systems then sintering temperatures above 1200 °C may cause some highly undesirable reactions with neighbouring materials.

The specific conductivities of screen-printed LSM layers on Al_2O_3 substrates, sintered at 1200 °C and 1300 °C, are shown in **Figure 6**. The electrical conductivity

was measured by the four-probe technique. The electrical conductivity of the sample sintered at 1300 °C and measured at 800 °C was found to be 60 S/cm, and for the sample sintered at 1200 °C, 35 S/cm. As expected, the results show that a higher sintering temperature increased the material's electrical conductivity. According to the literature, in samples sintered at 1400 °C the electrical conductivity is increased to 65 S/cm, exclusively due to the additional effect of densification (10). The relatively high measured specific electrical conductivity at 1300 °C (and even at 1200 °C)
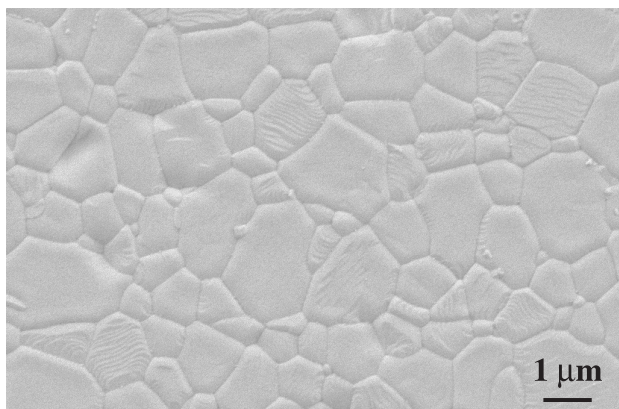
Figure 5: Microstructure of polished und thermally etched sample S1 after sintering at 1150 °C (the dense region)
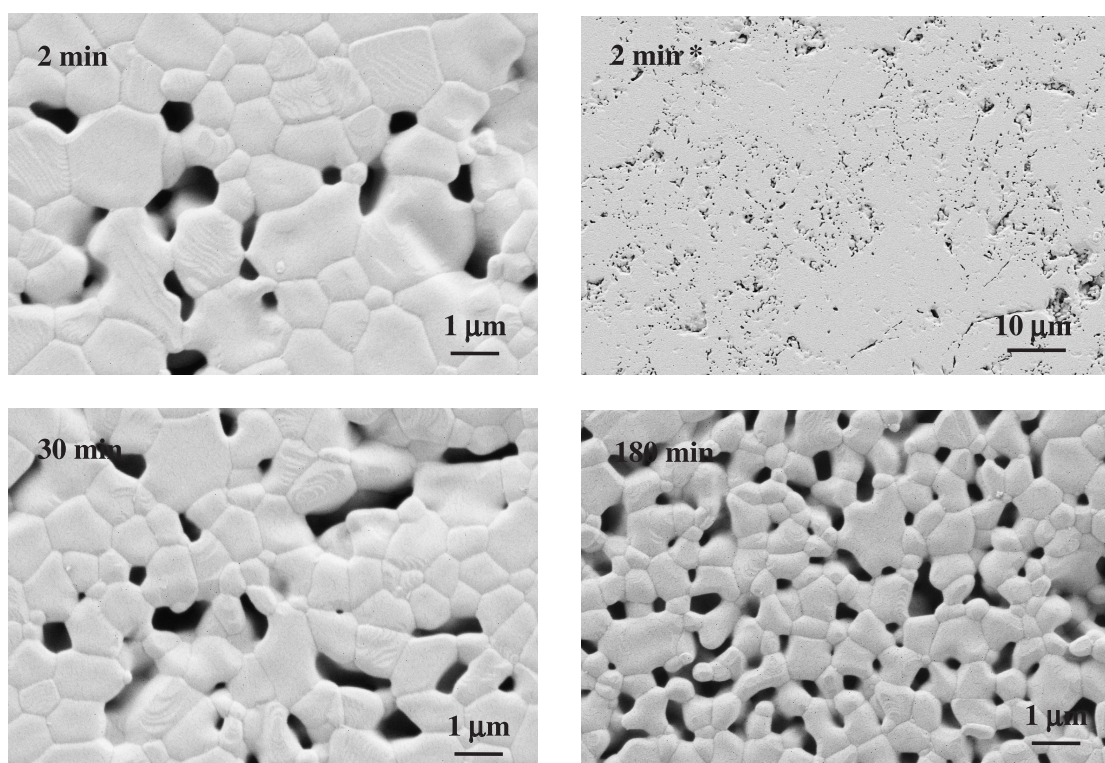**Slika 5:** Mikrostruktura vzorca S1 po sintranju (1150 °C), poliranju in termičnem jedkanju (gosto področje)
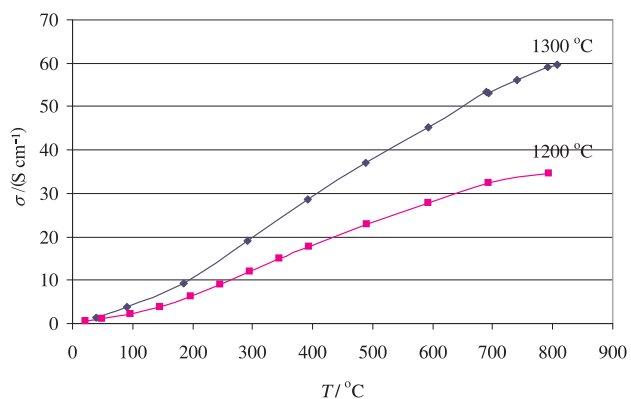
Figure 6: Measurements of specific electrical conductivity for samples sintered at 1200 °C and 1300 °C
Slika 6: Specifična električna prevodnost vzorcev, sintranih pri 1200 °C in 1300 °C

Figure 7: SEM micrographs of LSM material with the addition of the mass fraction 10 % pore former for different times of homogenization in the ball mill
Slika 7: SEM-posnetek materiala LSM z 10-odstotnim dodatkom por, ki so nastale pri različnih časih homogenizacije pri mletju

also means that good particle-to-particle contact had already been established at these temperatures.

Some special applications of LSM-based materials require not only excellent contact between the particles but also a relatively high open porosity. To test the ability to form such porous LSM bodies with good particle-to-particle contact, methyl cellulose as a pore-former was admixed prior to tablet shaping and sintering.

After methyl cellulose addition an increase in the porosity after different mixing times in the ball mill was observed for the sintered LSM samples containing mass fraction 10 % of pore former. The scanning electron micrographs in **Figure 7** show that for a mixing time of 2 minutes the sample is composed of dense and less-dense regions. Less-dense regions contain larger several-micrometre-sized pores, while the more-dense regions contain smaller micron or sub-micrometre pores. This relatively high inhomogeneity in the material microstructure is a consequence of an insufficient homogenization time. Using image-analysis software (Karl Zeiss KS 300 3.0) the porosity in the dense regions was estimated as 5.8 %, while the overall porosity (calculated from the material's geometrical density) reached 11.5 %. After 30 minutes of homogenization time the microstructure of the material still revealed differences in density throughout the sample, yielding 7 % porosity in dense regions and 23.9 % overall porosity.

A superb microstructure was achieved after 180 min of homogenization, with no substantial differences in the material's microstructure throughout the sample (33.7 % of overall porosity). Considering the fact that the electrical conductivity in the latter case still remains very close to that of the dense sample, such a microstructure could already be applied at the cathode site in a potential SOFC system.

4 CONCLUSIONS

LSM was synthesized by a non-conventional wet-chemical method. This co-precipitation route included mixed La-Sr-Mn carbonate preparation and its subsequent thermal treatment. Calcined LSM powders after treatment at 1000 °C were very crystalline, with only traces of secondary phases, which completely dissolved in the LSM perovskite structure after heating to 1200 °C. The sintering characteristics of the prepared LSM powders revealed that dense structures could be prepared at sintering temperatures as low as 1150 °C, but the problem of powder homogenization prior to sintering has still to be solved. The specific electrical conductivity of sintered LSM elements reached 35 S/cm (measured at 800 °C) after sintering at 1200 °C and 60 S/cm (measured at 800 °C) after sintering at 1300 °C. Such a relatively high electrical conductivity is believed to be a consequence of the good powder sinterability and hence

the excellent particle-to-particle contact. Homogeneous sintered bodies with a higher porosity, but still good contact between the particles, were achieved after admixing methyl cellulose as a pore former and a prolonged homogenization of 180 min in a ball mill, with subsequent sintering at 1200 °C.

5 REFERNECES

[1] N. Q. Minh, Ceramic Fuel Cells, J. Am. Ceram. Soc., 76 (**1993**) 563

[2] R. Mahesh, R. Mahendiran, A. K. Raychaudhuri, C. N. R. Rao, Effect of particle size on the giant magnetoresistance of $La_{0.7}Ca_{0.3}MnO_3$, Appl. Phys. Lett., 68 (**1996**), 2291

[3] Y. Huang, Z. Xu, C. Yan, Z. Wang, T. Zhu, C. Liao, Soft chemical synthesis and transport properties of $La_{0.7}Sr_{0.3}MnO_3$ granular perovskites, Solid State Commun., 114 (**2000**), 43

[4] N. Zhang, W. Ding, W. Zhong, D. Xing, Y. Du, Tunnel-type giant magnetoresistance in the granular perovskite $La_{0.85}Sr_{0.15}MnO_3$, Phys. Rev., B56 (**1997**), 8138

[5] L. Kilizendermann, D. Das, D. Bahadur, R. Weiss, H. Nikel, K. Hilpert, Chemical interaction between La-Sr-Mn-Fe-O based perovskites and yttria stabilized zirconia, J. Am. Ceram Soc., 80 (**1997**) 4, 909–914

[6] C. Clausen, C. Bagger, J. B. Bilde-Sorensen, A. Horsewell, Microstructural and microchemical characterization of the interface between $La_{0.85}Sr_{0.15}MnO_3$ and Y_2O_3-stablized ZrO_2, Solid State Ionics, 70/71 (**1994**), 59–64

[7] R. J. Bell, G. J. Millar, J. Drennan, Influence of synthesis route on the catalytic properties of $La_{1-x}Sr_xMnO_3$, Solid State Ionics, 131 (**2000**), 211

[8] J. Sefir, S. Vaucher, P. Holtappels, U. Vogt, H.-J. Schindler, J. Van herle, E. Suvorova, P. Buffat, D. Perret, N. Xanthopoulos and O. Bucheli, Characterization of perovskite powders for cathode and oxygen membranes made by different synthesis routes, Journal of the European Ceramic Society, 25 (**2005**), 1991–1995

[9] J. Tanaka, K. Takahashi, Y. Yajima, M. Tsukioka, Lattice constants of monoclinic ($La_{0.8}Ca_{0.2}$)MnO_3, Chemistry Letters, (**1982**), 1847

[10] A. Ghosh, A. K. Sahu, A. K. Gulnar, A. K. Suri, Synthesis and characterization of lanthanum strontium manganite, Scripta Materialia, 52 (**2005**), 1305–1309

THE EFFECT OF SILICA FUME ADDITIONS ON THE DURABILITY OF PORTLAND CEMENT MORTARS EXPOSED TO MAGNESIUM SULFATE ATTACK

VPLIV DODATKA SILICA FUME NA TRAJNOST CEMENTNIH MALT PORTLAND, IZPOSTAVLJENIH DELOVANJU MAGNEZIJEVEGA SULFATA

Jelica Zelić, Ivana Radovanović, Dražan Jozić

Faculty of Chemical Technology, University of Split, Teslina 10/5, HR-21 000 Split, Croatia
jelica.zelic@ktf-split.hr

The deterioration of concrete structures due to the presence of sulfate in soils, groundwater and marine environments is a well-known phenomenon. The use of blended cements incorporating materials such as natural pozzolans, fly ash or silica fume have an important role in the long-term durability of concrete exposed to sulfate attack. In this work, the partial replacement (mass fractions 2–15 %) of commercially blended Portland cement (Type CEM IIA-S 42.5N) with silica fume (SF) was investigated in terms of the resistance of SF mortars to a magnesium sulfate (MgSO$_4$) solution (ω(SO$_4$)$^{2-}$ = 2.5 %; exposure time up to 6 months at 20 °C). The changes in the length of the mortars due to expansion, as well as the changes in the elasticity modulus and mechanical strength loss as a function of silica fume replacement were determined. Structural changes in the mortars due to magnesium sulfate attack were also evaluated by differential thermal analysis (DTA) and by X-ray diffraction (XRD) analysis. The results show that the replacement of SF in most cases has a positive effect on the magnesium sulfate resistance. Mortars containing more than 8 % of mass fraction of SF replacement are characterized by a good sulfate resistance and show lower expansion than the control mortar on the basis of the sulfate-resisting Portland cement, due to the absence of the gypsum and ettringite, detected by the XRD analysis. It is also shown that the elastic modulus is proportional to the compressive strength, but higher compressive strength does not necessary correlate with a better resistance to sulfate attack.

Key words: blended cement, silica fume, sulfate attack, durability, elastic modulus

Propadanje strukture betona v okolju sulfata (tla, podzemne vode in morska voda) je znan pojav. Uporaba mešanih cementov z dodatki, kot so naravni pucolani, leteči pepel ali "silica fume" (SF), ima pomembno vlogo pri dolgotrajni trdnosti betona, izpostavljenega sulfatni koroziji. V tem delu je preučevan vpliv SF (masni delež 2–15 %) kot nadomestni dodatek industrijskemu portlandskemu cementu (CEM IIA-S 42.5N) na odpornost cementne malte proti delovanju raztopin magnezijevega sulfata (w(SO$_4$)$^{2-}$ = 2.5 %; čas izpostavljanja do 6 mesecev pri 20 °C). Merili smo naslednje parametre v odvisnosti od deleža SF: sprememba dolžine malt zaradi ekspanzije, spremembe modulov elastičnosti in izguba mehanične čvrstosti. Strukturne spremembe v maltah, izpostavljenih vplivu sulfatne korozije, smo spremljali z diferencialno termično analizo (DTA) in rentgensko difrakcijsko analizo (XRD). Rezultati kažejo, da nadomestni dodatek SF v večini primerov povečuje odpornost malt proti vplivu magnezijevega sulfata. Malte z masnim deležem dodatka SF, večjim od 8 %, so okarakterizirane kot dobro sulfatno odporne in kažejo manjšo ekspanzijo kot kontrolna malta na osnovi sulfatno odpornega portlandskega cementa, ker nimajo gipsa in etringita, kar je potrjeno z analizo XRD. Opaženo je tudi, da je modul elastičnosti proporcionalen kompresijski čvrstosti, toda večje kompresijske čvrstosti niso nujno povezane z večjo odpornostjo malt proti korozijskemu delovanju sulfata.

Ključne besede: mešani cement, «silica fume», sulfatna korozija, trajnost, modul elastičnosti

1 INTRODUCTION

Sulfate attack on cement concrete is a complex process and many factors such as cement type, sulfate cation type, sulfate concentration and exposure period can affect the sulfate resistance[1,2]. The sulfate ions react with the C$_3$A and Ca(OH)$_2$ in the concrete to produce expansive and/or softening types of deterioration associated with both the ettringite and gypsum formation. When the attacking solution contains Mg^{2+} ions, such as in magnesium sulfate (MgSO$_4$), the formation of magnesium hydroxide (brucite) and the conversion of the main cement hydrated product, calcium silicate hydrate (CSH gel), into magnesium silicate hydrate (MSH) are also observed[3-5]. Several ideas have been suggested to increase the resistance of

concrete against sulfate attack either by decreasing the porosity (high cement content, low water-to-cement ratio) or by using more resistant types of binders (sulfate-resisting Portland cement, addition of pozzolanas and blast furnace slag). Studies[3,6-11] have shown that the addition of pozzolans such as silica fume enhances the strength and durability of mortars exposed to sulfate attack. This improvement in sulfate resistance for the Portland cement–silica fume blended concrete/ mortars or pastes is attributed to the pore refining and pore refinement effect occurring due to a pozzolanic reaction between the calcium hydroxide liberated during the cement hydration process and the silica fume when a new CSH gel was formed. This CSH gel is more susceptible to the magnesium than to sodium sulfate attack. In the advanced stages of attack, therefore, the Ca

ions in the CSH can be completely replaced by Mg ions, leading to the decalcification of the CSH, and the loss of the cementitious structure[12].

The aim of the this work is to give a comparative evolution of the sulfate resistance and durability of SF-blended cement mortars immersed in 2.5 % magnesium sulfate solution, as well as to evaluate the optimum dosage level of silica fume replacement to minimize the deleterious effects of the Mg-sulfate attack.

2 EXPERIMENTAL

Commercial blended Portland cement, CEM IIA-S 42.5N (the Dalmacijacement, Croatia), that was produced by grinding cement clinker and mixing with up to 5 % of gypsum and about 25 % of blast furnace slag was used in this investigation. Its Blaine specific surface area was 3,530 cm^2/g. The Bogue composition of the cement clinker was (in mass fractions): C_3S = 64.7 %; C_2S = 9.6 %; C_3A = 7.5 %; C_4AF = 10.1 %. The silica fume was collected from the production of ferrosilicon (ex the Dalmacija Ferroalloys Works, Dugi Rat, Croatia), containing mass fraction of SiO_2 about 90 %, having a surface area of 18 m^2/g, as measured by the BET nitrogen adsorption method, with extremely fine spherical and amorphous particles[9,10]. The sulfate-resisting cement (the Dalmacijacement, Croatia), Type V according to the ASTM C-150, was used as the control cement. Salts $MgSO_4$ x $7H_2O$, p. a. were used in the preparation of the magnesium sulfate solution, $\omega(SO_4)^{2-}$ = 2.5 % (25,000 mg/L). The mortars were prepared from a mixture of blended cement, standard quartz sand and mass fractions of silica fume (0, 2, 5, 8, 11 and 15) %, according to the Croatian Standard HRN EN 196-1 : 2005. The mortar samples were designated as P-0, P-2, P-5, P-8, P-11 and P-15, respectively. The water-to-binder (cement+SF) ratio varied from 0.50 to 0.67; the samples were prepared to have the same flow-table consistency. No super-plasticizer was added. Two kinds of mortar samples were prepared: (i) for mechanical strength tests, prismatic specimens of dimensions (40 × 40 × 160) mm, according to the Croatian Standard HRN EN 196-1:2005; (ii) for the potential sulfate-resistance tests, and for the modulus of elasticity tests, prismatic specimens of dimensions (25.4 × 25.4 × 285.75) mm with two stainless-steel inserts cast into the ends to facilitate accurate monitoring of the changes in length, according to the ASTM C.452-68. After a 24-hour setting period in a humid environment (20 °C, 90 % RH), the specimens were taken out of the moulds and immersed into tap water for 27 d. The first tests were carried out 28 d after the sample preparation, and then the samples were exposed to a magnesium sulfate solution. The changes in the samples due to magnesium sulfate attack were measured after 28 d and every 28 d thereafter for a 180-day period. The structural changes in the samples during sulfate attack were identified by

X-ray diffraction analysis (XRD; a Philips PW 1010, Netherlands) with CuKα radiation in the ranges of Bragg's angles of 3–60° (2 theta). The quantity of calcium hydroxide and magnesium hydroxide (brucite) in the mortar samples during sulfate attack was determined by differential thermal analysis (DTA-DTG-TG; a Derivatograph MOM, Hungary).

3 RESULTS AND DISCUSSION

Figure 1 shows the compressive strength of the mortars exposed in the Mg-sulfate solution at room temperature. There was a continuous increase in compressive strengths with exposure time up to 90 d for all the SF-mortars, except the P-5 sample. After this period, the strengths decreased for all the samples exposed to sulfate attack. The increase observed in the compressive strengths for up to 90 d can be attributed to two types of reaction: (i) the continuous hydration of the unhydrated cement components to form more hydration products in addition to the reaction of SF (or slag from the blended cement used) with the liberated lime to form more CSH leading to increasing compressive strength, and (ii) the reaction of sulfate ions with the hydrated cement components to form gypsum and ettringite. Both reactions lead to a denser structure as a result of the precipitation of the reaction products within voids and micropores. After longer periods the magnesium sulfate attack becomes more dominant, leading to the formation of microcracks, which decreases the strength[11]. The results obtained also show that the sulfate resistance of these SF mortars seems to be slightly higher than the P-0 mortar, but lower than the control mortar based on the sulfate-resisting cement (designated SPC).

Figure 2 presents the results for the expansion of mortars exposed to the sulfate attack. It can be seen that the smallest expansion, even smaller than the control
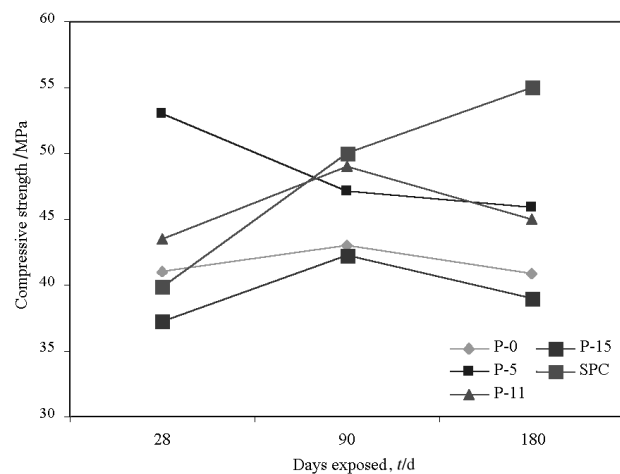
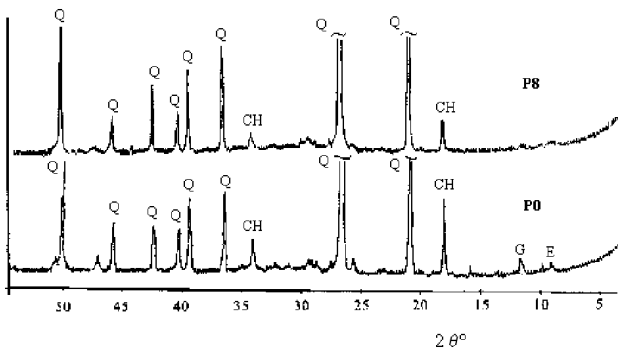**Figure 1:** Mortars' compressive strengths *vs.* exposure time to MgSO₄ solution
Slika 1: Kompresijska čvrstost malt *vs.* čas izpostavljanja raztopini MgSO₄
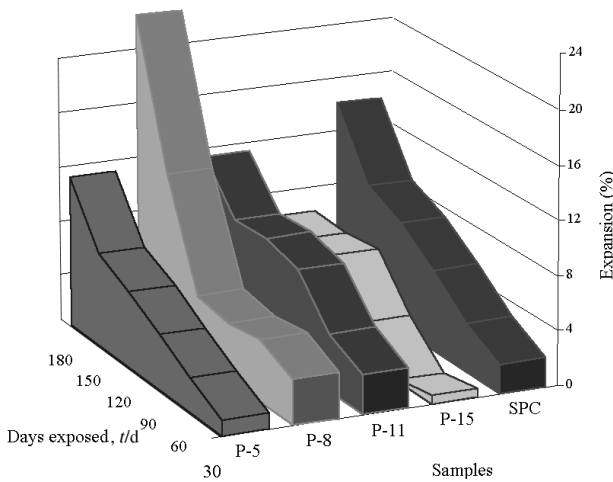
Figure 2: Expansions of mortars *vs*. exposure time to MgSO₄ solution
Slika 2: Ekspanzija malt *vs*. čas izpostavljanja raztopini MgSO₄

Figure 4: Variation of the dynamic modulus of elasticity with exposure time of mortars to MgSO₄ solution
Slika 4: Sprememba dinamičnega modula elastičnosti glede na časovno obdobje izpostavljanja malt v raztopini MgSO₄
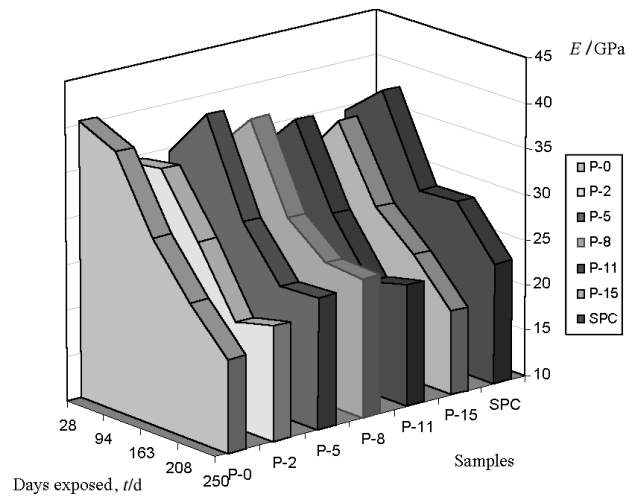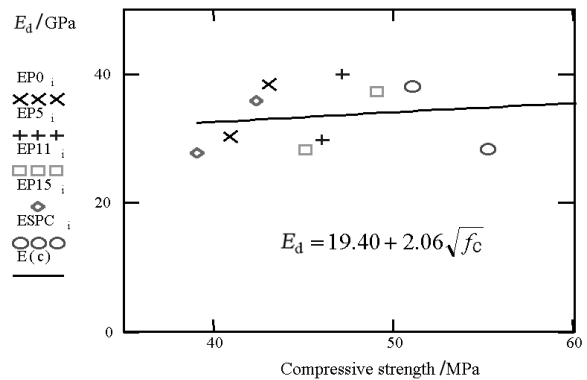
mortar on the basis of sulfate-resisting Portland cement (the SPC sample), comes from the samples containing mass fractions 11 % and 15 % of silica fume. The highest expansion of 107.82 % and 59.91 % and the intensive trend of the breakdown were observed in the sample without (P-0) and with 2 mass percent (P-2) of silica fume, respectively: the P-0 sample disintegrated after only 90 d, while the P-2 one lasted for 150 d of immersion in the MgSO₄ solution before breakdown due to corrosion[13]. The results obtained show that the greatest expansion was observed in the P-0 mortar, which did not exhibit the lowest compressive strength. The lack of correlation between the results of the compressive-strength measurements and the damage due to sulfate corrosion (microcracks) was also pointed out by other authors[14].

Figure 3 presents the XRD patterns of the P-0 and P-8 samples exposed to Mg-sulfate attack for 120 d. While the formation both of gypsum (G) and ettringite (E) as the result of sulfate corrosion is detected for the

P-0 sample, in the P-8 sample these corrosion products were not found.

Figure 4 presents the results of the changes in the elasticity modulus (E-modulus) of the mortars immersed in the Mg-sulfate solution, which were determined by measuring the dynamic resonance frequency. An electrosonometer[15] was used for this purpose. Details for the determination of the dynamic resonance frequency and for calculating the modulus of elasticity were described elsewhere[13,15]. It can be seen that all samples tend to show a continuous decrease in the E-modulus with the time of exposure. Mortars containing silica fume showed a similar or slightly higher E-modulus with respect to the mortar containing no silica fume (the P-0), but these samples showed a significant reduction in modulus with respect to the reference SPC mortars.

Figure 5 presents the E-modulus data mortars versus the square root of compressive strength for all the

Figure 3: XRD diffractograms of the P-0 and P-8 mortar samples exposed to MgSO₄ solution for 120 d, where Q-quartz, CH-lime, G-gypsum, E-ettringite
Slika 3: XRD-difraktogrami za vzorce malt P-0 in P-8 po 120 d izpostavljanja raztopini MgSO₄, kjer so: Q-kremen, CH-kalcijev hidroksid, G-gips, E-etringit

Figure 5: The dynamic modulus of elasticity *vs*. compressive strength for mortars exposed to MgSO₄ solution
Slika 5: Dinamični modul elastičnosti *vs*. kompresijska čvrstost za malte, izpostavljene delovanju raztopine MgSO₄
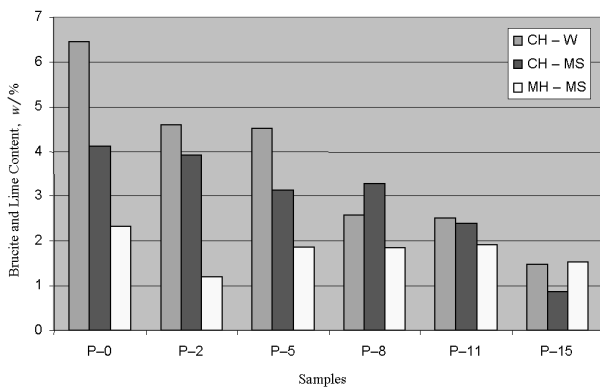
Figure 6: Lime and brucite content in the SF-mortar samples exposed to MgSO$_4$ solution for 120 d. Control SF-mortars are stored in tap water (designated CH-W)
Slika 6: Vsebnost kalcijevega hidroksida (CH) in brucita (MH) v vzorcih SF-malt po 120 d izpostavljanja raztopini MgSO$_4$. Kontrolni vzorci SF-malt so hranjeni v vodovodni vodi (označba CH-W)

mortars exposed to the MgSO$_4$ solution. Based on the experimental data following the correlation between the dynamic modulus of elasticity (E_d) and the compressive strength (f_c) was observed to be $E_d = 19.40 + 2.06 \sqrt{f_c}$, which is in good agreement with the relationship $E_d = 22 + 2.8 \sqrt{f_c}$, which is given in the British Standard B.S.CP 100:1972.

Figure 6 presents the results of the quantity of unleached lime and brucite formed in the specimens after 120 d of the magnesium sulfate immersion. The curve, designated W-CH, illustrated the relationship between the quantity of unleached lime and the SF replacement for samples cured in tap water[9,10]. More leaching in the MgSO$_4$ solution than in the water was demonstrated by the mortars with and without up to mass fraction 8 % of silica fume, suggesting that lime (calcium hydroxide) was converted to gypsum and brucite[4]. The presence of brucite, determined by DTA, in all the samples after 120 d of sulfate immersion was found, although the brucite formation was not observed by the XRD analysis. The relatively small concentration of brucite formed was related to the gypsum in the samples and explains why the observed XRD peaks due to brucite were always weak[16]. The presence of brucite obtained in the SF-mortar samples suggests a rapid attack by MgSO$_4$. However, as the pozzolanic reaction proceeded, the reduction in the permeability and the refinement of the pore structure overcame the negative effect of the sulfate attack.

4 CONCLUSIONS

Silica fume replacement enhances the durability of mortar exposed to magnesium sulfate attack due to the lowering of the lime content, and therefore the increase

of the initial compressive strength, on account of the pozzolanic reaction. Thereafter, by the decreasing of lime content in mortars during the Mg-sulfate immersion the formation of gypsum and ettringite, which are responsible for the decreasing of mortar durability, decreases. Mortars containing the mass fraction more than 8 % of silica fume replacement are characterized by a good sulfate resistance and show lower expansion than a control sulfate-resisting mortar due to the absence of gypsum and ettringite, detected by XRD analysis. Although the formation of brucite, determined by DTA analysis, suggests a rapid attack by MgSO$_4$ solution and an affect on the compressive strength of SF-mortars, the pozzolanic reaction (reduction in permeability and refinement of the pore structure) overcame this negative effect. The elastic modulus is proportional to the compressive strength, but a higher compressive strength does not necessarily correlate with a better durability to sulfate attack. For these experimental conditions, the optimum dosage level of 15 % silica fume replacement to minimize the deleterious effects of magnesium sulfate attack can be proposed.

5 REFERENCES

[1] A. Neville, Cem. Concr. Res. 34 (**2004**), 1275–1296

[2] F. Bellmann, B. Möser, J. Stark, Cem. Concr. Res. 36 (**2006**), 358–363

[3] M. D. Cohen, A. Bentur, ACI Mater. J. 83 (**1988**), 147–157

[4] R. S. Gallop, H. F. W. Taylor, Cem. Concr. Res. 26 (**1996**), 1013–1028

[5] P. K. Mehta, Cem. Concr. Res. 13 (**1983**), 401–406

[6] K. Torii, M. Kawamara, Cem. Concr. Res. 24 (**1994**), 361–370

[7] P. S. Mangat, J. M. Khatib, ACI Mater. J. 92 (**1995**), 542–552

[8] F. Türker, F. Aköz, S. Koral, N. Yüzer, Cem. Concr. Res. 27 (**1997**), 205–214

[9] E. Tkalčec, J. Zelić, Zement-Kalk-Gips 11 (**1987**), 574–579

[10] J. Zelić, R. Krstulović, E. Tkalčec, P. Krolo, Cem. Concr. Res. 29 (**1999**), 819–826

[11] E. E. Hekal, E. Kishar, H. Mostafa, Cem. Concr. Res. 32 (**2002**), 1421–1427

[12] M. Santhanan, M. D. Cohen, J. Olek, Cem. Concr. Res. 33 (**2003**) 341–346.

[13] I. Radovanović, Diploma Thesis, Faculty of Chemical Technology, University of Split, 2004

[14] E. F. Irassar, A. Di Maio, O. R. Batic, Cem. Concr. Res. 26 (**1996**), 113–123

[15] D. Tončić, P. Gugić, I. Mandić, Croatian J. Cem. Ind. 1 (**1982/83**), 3–6

[16] S. A. Hortshorn, J. H. Sharp, R. N. Swamy, Cem. Concr. Res. 29 (**1999**), 1331–1340

ACTIVATED SINTERING OF MAGNESIUM OXIDE OBTAINED FROM SEAWATER

AKTIVIRANO SINTRANJE MAGNEZIJEVEGA OKSIDA, DOBLJENEGA IZ MORSKE VODE

Vanja Martinac, Miroslav Labor, Meri Mirošević-Anzulović, Nedjeljka Petric

Faculty of Chemical Technology, Department of Thermodynamics, Teslina 10/V, 21000 Split, Croatia
martinac@ktf-split.hr

The process of isothermally sintering magnesium oxide obtained from seawater by substoichiometric (where precipitation of magnesium hydroxide took place with 80 % of the stoichiometric quantity of dolomite lime) and by overstoichiometric precipitation (which took place with 120 % of the stoichiometric quantity of dolomite lime) was examined, with the addition of mass fractions (1, 2 and 5) % TiO_2, at temperatures in the range 1550–1750 °C, with (1, 3 and 5) h of soaking at the maximum temperature. The process was followed by a determination of the product density, as well as of the B_2O_3 content in the sintered samples. The results indicate that, besides favorably affecting the density of the sintered samples, the addition of TiO_2, with increasing temperature and soaking time, also significantly reduces the B_2O_3 content in the sintered magnesium oxide obtained from seawater. A statistical analysis of the obtained data was performed with the "Statistica" package in order to obtain a model of the density (ρ) of sintered samples of magnesium oxide relative to the temperature (t), time of isothermal heating (τ), and the percentage of added TiO_2 (w).

Key words: substoichiometric precipitation, overstoichiometric precipitation, magnesium oxide from seawater, TiO_2 addition, activated sintering

Proučevan je proces izotermnega sintranja magnezijevega oksida, dobljenega iz morske vode z nestehiometrijskim (dodatek dolomitnega apna je bil 80 % od stehiometrijsko potrebne količine) in prestehiometrijskim usedanjem (z dodatkom 120 % od stehiometrijske količine dolomitnega apna) z dodatkom masnih deležev TiO_2 (1, 2 in 5) %, v temperaturnem intervalu 1550–1750 °C, v trajanju izotermnega sintranja (1, 3 in 5) h. Proces je bil spremljan z določevanjem gostote in določevanjem vsebnosti B_2O_3 v sintranih vzorcih. Rezultati preučevanja kažejo, da dodatek TiO_2 pozitivno deluje na gostoto sintranih vzorcev, s povečanjem temperature in obdobjem izotermnega sintranja pa občutno vpliva tudi na zmanjšanje B_2O_3 v sintranem magnezijevem oksidu, dobljenem iz morske vode. Da bi dobili model odvisnosti gostote (ρ) sintranih vzorcev magnezijevega oksida od temperature (t) in časa izotermnega sinteriranja (τ), ter deleža dodanega TiO_2 (w) je bila narejena statistična obdelava dobljenih podatkov z uporabo paketa "Statistica".

Ključne besede: nestehiometrijsko usedanje, prestehiometrijsko usedanje, magnezijev oksid iz morske vode, TiO_2 dodatek, aktivirano sintranje

1 INTRODUCTION

Magnesia[1] (MgO) is a very important material for the refractory industry. Due to its high refractory properties (MgO melts at (2823 ± 40) °C), MgO ceramics are chemically inert, resistant to the effect of metal melts, acid gases, alkali slag, neutral salts, and react with carbon only above 1800 °C. Raw magnesites for refractory use are obtained from natural ore or are synthetically processed from seawater. Magnesium oxide obtained from seawater[2-9] is a high-quality refractory material, and its advantages lie not only in the huge reserves of seawater[10] (1 m^3 contains 0.945 kg of magnesium), but in the higher purity of the sintered magnesium oxide (> 98 % MgO). The magnesium oxide used here was obtained from seawater either by substoichiometric (MgO 80 % pptn – where pptn stands for precipitation) or overstoichiometric (MgO 120 % pptn) precipitation of magnesium hydroxide in seawater using dolomite lime.

The purpose of this work was to examine the effect of TiO_2 additions on the properties (density and the B_2O_3 content) of sintered samples of magnesium oxide obtained from seawater at elevated temperatures. The examinations described were carried out in order to obtain a model of the density of sintered samples of magnesium oxide relative to the temperature and the time of isothermal heating and the percent of added TiO_2.

2 EXPERIMENTAL

The composition of the seawater used for the precipitation of magnesium hydroxide was:
MgO = 2.124 g dm^{-3}; CaO = 0.5573 g dm^{-3}

The composition of the dolomite lime used as the precipitation agent was as follows (mass fractions, w/%):
CaO = 57.17 % MgO = 42.27 %
SiO$_2$ = 0.099 % Al$_2$O$_3$ = 0.051 %
Fe$_2$O$_3$ = 0.079 %

The experimental procedure used to obtain magnesium hydroxide from seawater was similar to that employed in our previous investigations[8,9]. The sedimentation rate was increased by the addition of the

optimum amount of the anionic 818A flocculent (polyacrylamide), produced by the Dutch firm Hercules. The experimental procedure used to determine the optimum quantity of the anionic 818A flocculent has been described in a previous study[11]. The magnesium hydroxide obtained from seawater was dried at 105 °C and then calcined at 950 °C. The composition of the magnesium oxide obtained by precipitation with 80 % of the stoichiometric quantity of dolomite lime was (mass fractions, w/%): 98.76 % MgO, 0.88 % CaO and 0.1934 % B_2O_3.

The composition of the magnesium oxide obtained by precipitation with 120 % of the stoichiometric quantity of dolomite lime was (mass fractions, w/%): 97.92 % MgO , 1.45 % CaO and 0.1055 % B_2O_3.

Mixtures of magnesium oxide were then prepared with the addition of a mass fraction of 1 %, 2 % and 5 % TiO_2. The doping oxide used was analytical reagent grade titanium (TiO_2 p. a.) in the rutile form, produced by Merck. The samples were homogenized by manual stirring in absolute ethanol (C_6H_5O p. a.). The mixtures were cold pressed into compacts in a hydraulic press at a pressure of 625 MPa. The compacts were then sintered in a gas furnace, made by a French firm Mecker (type 553), with a zirconium (IV)-oxide lining, at 1550 °C, 1650 °C and 1750 °C with 1h, 3h and 5h of soaking at the maximum temperature.

It took approximately 2 h to reach the maximum temperature in the furnace. After sintering, the samples were left to cool in the furnace. The sample density after sintering (ρ) was determined from the volume of water displaced from a calibrated cylinder. The boron content in the magnesium oxide samples examined was determined potentiometrically. The variation coefficient for the method used was ± 1 %[12]. The results shown represent the average of a number of measurements.

3 RESULTS AND DISCUSSION

Tables 1 and 2 show the experimentally obtained values for the density under the operating conditions described for sintered magnesium oxide samples (80 % precipitation) and magnesium oxide samples (120 % precipitation). The results indicate that at higher temperatures, such as 1550 °C, 1650 °C and 1750 °C, the increase in the density of the samples of magnesium oxide obtained from seawater is not very significant when compared to the un-doped samples, even though they were sintered under the same thermal conditions. Therefore, at higher temperatures in the range 1550–1750 °C, the effect of the TiO_2 addition is less evident because the concentration of the added ions is evenly distributed over the whole grain mass. One can assume that the mass transfer is the same as with pure MgO, determined by the diffusion of O^{2-} ions through the MgO lattice as the slower diffusion species. The increased temperature leads to the increased mobility of the elements forming the crystal lattice, a contact surface

Table 1: Density (ρ) of sintered magnesium oxide samples (80 % precipitation) with the addition of a mass fraction of 1 %, 2 % and 5 % TiO_2, and no sintering aid, t = 1550 °C, 1650 °C, 1750 °C, τ = 1 h, 3 h, 5 h, p = 625 MPa
Tabela 1: Gostota (ρ) za sintrane vzorce magnezijevega oksida (80-odstotno usedanje) z masnimi deleži TiO_2 in 1, 2 in 5 %, in brez dodatka TiO_2, t = 1550 °C, 1650 °C, 1750 °C, τ = 1 h, 3 h, 5 h, p = 625 MPa

| sample | t/°C | τ/h | ρ/(g cm⁻³) | | | |
| | | | TiO₂ addition, w/% | | | |
			no sint. aid	1 %	2 %	5 %
80 % pptn	1550	1	3.2401	3.2691	3.3243	3.3361
		3	3.3181	3.3498	3.3439	3.3744
		5	3.3514	3.3643	3.3953	3.4017
	1650	1	3.3463	3.3798	3.4115	3.4257
		3	3.3513	3.3803	3.4245	3.4351
		5	3.4230	3.4128	3.4385	3.4510
	1750	1	3.3522	3.4007	3.4199	3.4391
		3	3.3660	3.4593	3.4513	3.4719
		5	3.4244	3.4881	3.4933	3.5289

Table 2: Density (ρ) of sintered magnesium oxide samples (120 % precipitation) with the addition of a mass fraction of 1 %, 2 % and 5 % TiO_2, and no sintering aid, t = 1550 °C, 1650 °C, 1750 °C, τ = 1 h, 3 h, 5 h, p = 625 MPa
Tabela 2: Gostota (ρ) za sintrane vzorce magnezijevega oksida (120-odstotno usedanje) z masnimi deleži TiO_2 in 1, 2 in 5 %, in brez dodatka TiO_2, t = 1550 °C, 1650 °C, 1750 °C, τ = 1 h, 3 h, 5 h, p = 625 MPa

| sample | t/°C | τ/h | ρ/(g cm⁻³) | | | |
| | | | TiO₂ addition, w/% | | | |
			no sint. aid	1 %	2 %	5 %
120 % pptn	1550	1	3.2880	3.3088	3.3980	3.4036
		3	3.3179	3.3557	3.4156	3.4383
		5	3.3739	3.3887	3.4409	3.4619
	1650	1	3.3350	3.3726	3.4253	3.4357
		3	3.3570	3.4029	3.4378	3.4603
		5	3.4244	3.4412	3.4662	3.5047
	1750	1	3.3711	3.4033	3.4292	3.4473
		3	3.4153	3.4516	3.4860	3.5180
		5	3.4591	3.4786	3.5018	3.5434

is formed between the particles of compacted powder, the porosity is eliminated, and the whole system shrinks[13-15]. **Tables 3 and 4** show the results of the examination of the effect of TiO_2 on the boron content in the sintered magnesium oxide samples (80 % and 120 % precipitation) for the operating conditions described. The results indicate that the TiO_2 addition significantly influences the reduction of the B_2O_3 content in the process of the isothermal sintering of magnesium oxide from seawater, even at higher temperatures. The different behavior of the magnesium oxide obtained by 80 % from that obtained by 120 % precipitation of magnesium hydroxide in seawater is due to the different contents of CaO in these samples. CaO retains the B_2O_3 in the samples during sintering. With MgO (120 % precipitation) the CaO content is much higher (w = 1.45 %) than with MgO (80 % precipitation) (w = 0.88 %),

Table 3: Effect of TiO_2 on B_2O_3 content in the sintered magnesium oxide samples (80 % precipitation) at t = 1550 °C, 1650 °C, 1750 °C, τ = 1 h, 3 h, 5 h, p = 625 MPa
Tabela 3: Vpliv TiO_2 na vsebnost B_2O_3 v sintranih vzorcih magnezijevega oksida (80-odstotno usedanje) pri t = 1550 °C, 1650 °C, 1750 °C, τ = 1 h, 3 h, 5 h, p = 625 MPa

sample	t/°C	τ/h	B_2O_3, w/%			
			TiO_2 addition, w/%			
			no sint. aid	1 %	2 %	5 %
80 % pptn	1550	1	0.1894	0.1249	0.0913	0.0245
		3	0.1337	0.1075	0.0193	0.0174
		5	0.0759	0.0637	0.0145	0.0132
	1650	1	0.1445	0.0750	0.0272	0.0216
		3	0.1020	0.0640	0,0161	0.0096
		5	0.0589	0.0257	0.0138	0.0085
	1750	1	0.0862	0.0594	0.0193	0.0158
		3	0.0415	0.0261	0.0116	0.0074
		5	0.0319	0.0126	0.0090	0.0055

and favors the $Ca_2B_2O_5$ formation reaction. In a previous paper[16] the X-ray diffraction method was used to prove the content of di-calcium borate ($Ca_2B_2O_5$) in sintered samples of magnesium oxide from seawater. Therefore, in the process of sintering, B_2O_3 reacts with CaO to form $Ca_2B_2O_5$. In papers[17-20] the X-ray diffraction method and EDAX analysis have helped determine that during the sintering process the added TiO_2 reacts with CaO from the solid MgO-CaO solution and forms calcium titanate $CaTiO_3$. Thus, TiO_2 binds a part of the CaO in the $CaTiO_3$ and as a result reduces the content of CaO that reacts with B_2O_3. In this way a smaller quantity of $Ca_2B_2O_5$ remains in the sintered sample, i.e., a higher quantity of B_2O_3 evaporates.

With MgO (120 % precipitation) there is an excess of CaO, which favors the formation of $Ca_2B_2O_5$, while with MgO (80 % precipitation) a larger part of the B_2O_3 evaporates from the sample into the air during sintering. A positive effect of the TiO_2 addition on the reduction of the B_2O_3 content in the magnesium oxide obtained from seawater makes it possible to achieve a high-purity product, because the hot-strength properties of certain refractory products are significantly affected by their boron content.

The results shown in **Tables 1 and 2** have also been considered in a regression analysis. The "Statistica" package was used to analyze statistically the data obtained, in order to obtain a model of the density of the sintered samples of magnesium oxide relative to the temperature (t), the time of isothermal sintering (τ), and the mass fraction of TiO_2 added (w).

A model of multiple regression has been proposed, $\rho = \beta_o + \beta_1 t + \beta_2 \tau + \beta_3 \ln (w+1) + \varepsilon$ for MgO samples (80 % precipitation) and for MgO samples (120 % precipitation), where ρ is the density (g cm^{-3}), t is the temperature (°C), τ is the time of isothermal sintering (h), w is the mass fraction (%) of added TiO_2, β_o, β_1, β_2, β_3 are

unknown coefficients, and ε is the random error in the model.

Table 4: Effect of TiO_2 on B_2O_3 content in the sintered magnesium oxide samples (120 % precipitation) at t = 1550 °C, 1650 °C, 1750 °C, τ = 1 h, 3 h, 5 h, p = 625 MPa
Tabela 4: Vpliv TiO_2 na vsebnost B_2O_3 v sintranih vzorcih magnezijevega oksida (120-odstotno usedanje) pri t = 1550 °C, 1650 °C, 1750 °C, τ = 1 h, 3 h, 5 h, p = 625 MPa

sample	t/°C	τ/h	B_2O_3, w/%			
			TiO_2 addition, w/%			
			no sint. aid	1 %	2 %	5 %
120 % pptn	1550	1	0.0705	0.0618	0.0360	0.0222
		3	0.0582	0.0354	0.0264	0.0119
		5	0.0312	0.0270	0.0245	0.0058
	1650	1	0.0592	0.0405	0.0331	0.0148
		3	0.0315	0.0286	0.0254	0.0068
		5	0.0180	0.0171	0.0106	0.0055
	1750	1	0.0331	0.0312	0,0216	0.0093
		3	0.0177	0.0119	0,0106	0.0046
		5	0.0148	0.0100	0.0084	0.0032

Table 5: Correlation matrix for MgO (80 % precipitation) samples
Tabela 5: Matrica korelacije za vzorce MgO (80 – odstotno usedanje)

variable	correlations (MgO (80 % pptn) samples)			
	t/°C	τ/h	TiO_2 addition, w/%	density, ρ/(g cm^{-3})
t/°C	1.00	0.00	-0.00	0.69
τ/h	0.00	1.00	-0.00	0.46
TiO_2 addition, w/%	-0.00	-0.00	1.00	0.43
density, ρ/(g cm^{-3})	0.69	0.46	0.43	1.00

Table 6: Correlation matrix for MgO (120 % precipitation) samples
Tabela 6: Matrica korelacije za vzorce MgO (120 – odstotno usedanje)

variable	correlations (MgO (120 % pptn) samples)			
	t/°C	τ /h	TiO_2 addition, w/%	density, ρ/(g cm^{-3})
t/°C	1.00	0.00	-0.00	0.53
τ/h	0.00	1.00	-0.00	0.51
TiO_2addition, w/%	-0.00	-0.00	1.00	0.60
density, ρ /(g cm^{-3})	0.53	0.51	0.60	1.00

Tables 5 and 6 show the correlation matrices for the examined samples. The results indicate that there is no correlation between the independent variables (temperature t, time τ and percentage of addition of TiO_2).

The estimate for the regression function for MgO (80 % precipitation) is: $\hat{\rho}$ = 2.461 + 0.000512 T + 0.0173 τ + + 0.0434 ln (w + 1) where s = 0.01899; R^2 = 0.9057; $F(3, 104)$ = 333.2251; p = 0.00

The estimate for the regression function for MgO (120 % precipitation) is: $\hat{\rho}$ = 2.686 + 0.000382 T + + 0.0181 τ + 0.0567 ln (w + 1) where s = 0.01413; R^2 = 0.9433; $F(3, 104)$ = 576.8233; p = 0.00

The regression functions and the regression coefficients are significant at the level of $p = 0.00$ in both models. The statistical analysis indicates that these models are useful for an estimation of the density of the samples examined.

4 CONCLUSIONS

The statistical analysis using the Statistica package indicates that the proposed models are useful and acceptable for an estimation of the density of the sintered magnesium oxide samples relative to the temperature (t), the time of the isothermal heating (τ), and the percent of added TiO_2 (w).

The favorable effect of the TiO_2 addition on the reduction of the B_2O_3 content in the sintered magnesium oxide obtained from seawater is due to two interdependent reactions of the formation of $Ca_2B_2O_5$ and $CaTiO_3$, which lead to a reduction in the B_2O_3 content during sintering.

5 LITERATURE

[1] Shand M. A., The Chemistry and Technology of Magnesia, Willey Interscience, N.York, 2006

[2] Frith M., Buttrey T., Strawbridge I., Brit. Ceram. Trans., 97 (**1998**), 29

[3] Sims C., Industr. Minerals, 7 (**1997**), 21

[4] Gilpin W. C., Heasman N., Chem. Ind., 16 (**1977**), 567

[5] Heasman N, Gas Wärme International, 28 (**1979**), 392

[6] Rabadžhieva D., Ivanova K., Balarev Hr., Trendafelov D., Žurnal priklačnoji himii, 70 (**1997**), 375

[7] Bonney O. V., U. S. Patent 43 148 85 (to Amstar Corporation, New York) 9 Feb. 1982, Chem. Abstr. 96 (**1982**), 125549

[8] Petric B., Petric N., Ing. Eng. Chem. Des. Dev., 19 (**1980**), 329

[9] Martinac V., Labor M., Petric N., Mater. Chem. Phys., 46 (**1996**), 23

[10] Brown E. et al., Seawater: Its composition, properties and behaviour, Butterworth Heinemann in association with The Open University, Walton Hall, Milton Keynes, 2nd Ed., 1997, 86

[11] Petric N., Martinac V., Labor M., Jurin O., Kovine zlit. tehnol., 33 (**1999**), 475

[12] Culkin F., The major constituents of seawater, in: Chemical Oceanography, Ed. by Riley J. P., Skirrow G., Vol.1, Academic Press, London, 1975, 136–151

[13] German R. M., Sintering theory and practice, Wiley, New York, 1996

[14] Kang Suk-Joong L., Sintering, Elsevier, 2005

[15] Lee Y. B., Park H. C., OH K. D., J. Mat. Sci., 33 (**1998**), 4321

[16] Petric N., Petric B., Tkalčec E., Martinac V., Bogdanić N., Mirošević-Anzulović M., Sci. Sinter., 19 (**1987**), 81

[17] Chaudhuri M. N., Kumar A., Bhadra A. K., Banerjee G., Sarkar S. L., Ceram. Bull., 71 (**1992**), 345

[18] Chaudhuri M. N., Kumar A., Bhadra A. K., Banerjee G., Interceram., 39 (**1990**), 26

[19] Ćosić M., Pavlovski B., Tkalčec E., Sci. Sinter., 21 (**1989**), 161

[20] Čeh M., Kolar D., J. Mater. Sci., 29 (**1994**), 6295

FLOWING OF THE MELT THROUGH CERAMIC FILTERS

PRETOK TALINE SKOZI KERAMIČNE FILTRE

Jiří Bažan[1], Karel Stránský[2]

[1]Technical University of Mining and Metallurgy in Ostrava, FMMI, 17. listopadu 15, 708 33 Ostrava-Poruba, Czech Republic
[2]VUT Brno, FSI, Technická 2, 619 69 Brno, Czech Republic
jiri.bazan@vsb.cz

It is important to clean melts by filtering them with ceramic filters. Particular attention must be paid to the hydraulic conditions as the melt flows through the filter. The Bernouilli equation is used to describe the filtration of the melts. The physical regularities of the capillary melt can be seen in the flow. The Hagen-Poiseuille law and Darcy's law have been applied. The characteristics of laminar flow have been examined, as have the attributes of turbulent flow. There are dimensionless criteria characterising the melt flow through a ceramic filter. The principal mechanisms of melt filtration are assessed.

Key words: metal melt, filtration, ceramic filter, flow of metals through pores, laminar and turbulent flow

Pomembnost čiščenja kovinske taline s filtriranjem skozi keramični filter. Hidravlični pogoji pretoka taline skozi filter. Uporaba Bernouillijeve enačbe za opis filtriranja taline. Fizikalne zakonitosti kapilarnega toka taline. Hagen-Poiseuillejev in Darcyjev zakon. Značilnosti laminarnega toka. Atributi turbulentnega toka. Brezdimenzijska merila, karakteristična za pretok taline skozi keramični filter. Glavni mehanizmi filtriranja kovinskih talin.

Ključne besede: kovinska talina, filtriranje, keramični filter, pretok taline skozi pore, laminarni in turbulentni pretok

1 INTRODUCTION

Recently, many laboratory-, pilot- and industrial-scale tests were carried out in the field of filtration using the casting of cast irons and steels. The results showed that the filtration of the melts of these metallic alloys can be used advantageously in melting foundries and steel shops, using the bottom pouring of steel (i.e., ladles with a taphole at the bottom), as well as in tundish metallurgy during the continuous casting of steel, and in cases when the ceramic filter is applied directly in the entry part of the inlet system during the casting of steel and cast iron.

2 FLOWING A MELT THROUGH THE CERAMIC FILTER

The overall efficiency of filtration technology is significantly influenced by the hydraulic conditions during the flowing of the melt through a ceramic filter. The basis for the description and evaluation of the hydraulic conditions during the flowing of a metallic melt (steels and cast irons) through a ceramic filter is the Bernouilli equation, expressing the principle of the conservation of mechanical energy of the flowing liquid [1]. It is possible to express the Bernouilli law for an ideal liquid considering the individual energies in the following equation

$$\frac{\rho \cdot v^2}{2} + h \cdot \rho \cdot g + p = const. \text{ /Pa} \qquad (1)$$

in which the term $(\rho \cdot v^2/2)$/Pa represents the kinetic energy of a unit volume of liquid, the term $(h \cdot \rho \cdot g)$/Pa represents the position or gravitational energy of a unit volume of liquid, given by the earth's gravity, and the term p/Pa represents the potential pressure energy of a unit volume of liquid, which is usually dependent on externally acting forces. The individual quantities in the equation are as follows: v, the flow velocity of an ideal liquid (m s^{-1}); ρ, the density of the flowing liquid (kg m^{-3}); h, the true position, i.e., the real height of the flowing unit volume of liquid (m); g, the acceleration due to gravity (m s^{-2}); and p, the pressure of a unit volume of flowing liquid in (Pa), the basic dimensions of which are kg s^{-2} m^{-1}. According to the Bernouilli equation the sum of the kinetic, positional and pressure energies of an ideally flowing liquid remains constant at each point in the flow.

However, if this equation is to be used for a description of the flow of a real liquid, e.g., the melts of steels and cast irons, it is necessary to add to the three terms on the left-hand side of the equation one more term, i.e., e_z, which expresses the loss of energy per unit volume of a real liquid, i.e., of the melt of steel or cast iron. The loss of energy during the flow of a real liquid through the filter will be directly proportional to the kinematic viscosity of the liquid, v (m² s^{-1}), to the velocity of the flowing liquid, v (m s^{-1}), indirectly proportional to the structure of the filter characterised by the length, the dimension and the geometry of the holes and capillaries in the filter, d/m, to the melt density, ρ/(kg m^{-3}), and to the dimensionless proportion constant, ξ. It is therefore necessary to express the Bernouilli

equation for a filtered melt of steel or cast iron in the following form:

$$\frac{\rho \cdot v^2}{2} + h \cdot \rho \cdot g + p + e_z = const. \text{ /Pa} \qquad (2)$$

or in the explicit form

$$\frac{\rho \cdot v^2}{2} + h \cdot \rho \cdot g + p + \frac{\xi \cdot v \cdot v \cdot \rho}{\delta} = const. \text{ /Pa} \qquad (3)$$

The flow of a liquid in a round hole (i.e., in a capillary), which is characteristic for direct holes (strainer filters), is governed by the Hagen-Poiseuille law, indicating that the flow volume of a viscous liquid during laminar flow through the tube of circular cross-section is directly proportional to the hydraulic gradient, $\Delta p/\Delta l$, and the fourth power of the tube radius, and indirectly proportional to the dynamic viscosity of the flowing liquid. The Hagen-Poiseuille law is written in the form:

$$Q_v/(\text{m}^3.\text{s}^{-1}) = \frac{\pi \cdot r^4 \cdot \Delta p}{\Delta l \cdot 8\eta} \qquad (4)$$

in which Q_v is the volume of liquid flowing through the tube, r/m is the internal radius of the tube (i.e., the capillary), $\eta/(\text{kg m}^{-1} \text{ s}^{-1})$ is the dynamic viscosity, Δp is the loss of static pressure along the length of the tube and Δl is the length of the tube. The hydraulic gradient, $(\Delta p/\Delta l)/(\text{kg m}^{-2} \text{ s}^{-2})$, is in this case a measure of the liquid's resistance to flow and it is proportional to the first power of the mean velocity of the liquid flowing through the capillary.

The Hagen-Poiseuille law also determines implicitly the mean velocity of the liquid flowing through the tube. The dependence of the mean velocity of the laminar flow in a capillary can be expressed by the equation obtained by dividing the flow volume, Q_v, by the area of the cross-section of the capillary, πr^2 :

$$v/(\text{m}.\text{s}^{-1}) = \frac{r^2 \cdot \Delta p}{\Delta l \cdot 8\eta} \qquad (5)$$

It follows from this equation that the mean velocity of the laminar flow through a capillary increases with the square of the capillary's radius; it is also directly proportional to the hydraulic gradient and indirectly proportional to the octuple of the value of the dynamic viscosity.

These relations are useful for an evaluation of the hydraulic conditions during the flow of melts of steel and ductile iron through ceramic filters, because they determine the causal relations between the physical quantities that characterise the melt, such as the viscosity and the density, the geometric characteristics of the filter, such as the diameters of the holes, the filter's thickness, the parameters of the flow of the melt through the filter, such as the flow volume of the melt, its flow-rate and also its hydraulic gradient in the filter.

The Darcy law is a special case of the Hagen-Poiseuille law. It expresses the velocity of the laminar flow of a liquid in a porous environment. According to this law the velocity of the flow in a porous environment is given by the linear relation

$$v_{\text{lam}}/(\text{m s}^{-1}) = k \frac{\Delta p}{\Delta l} \qquad (6)$$

where $k/(\text{m}^3 \text{ s kg}^{-1})$ is the coefficient of leakage (filtration) and $\Delta p/\Delta l$ is the already-mentioned hydraulic gradient. The Darcy law expresses the penetration of the melt into the pores in the walls of the ceramic filter's capillaries during filtration, which determines the physical-chemical reactions between the flowing melt and the filter ceramics.

2.1 Laminar flow

The laminar flow of a real liquid through the capillary is distributed in such a way that the maximum of the flow velocity is achieved in the axis of the circular section of the capillary and the minimum velocity (in practice, a zero flow velocity) near the capillary walls. The distribution of the flow velocity in the capillary in this case approaches the shape of a rotating paraboloid. This distribution of velocity occurs because the outermost layers of the liquid stick to the capillary walls, since there is great friction between the wall and the flowing liquid (in practice, an almost infinitely large friction) and due to the internal liquid friction, individual layers of liquid mutually obstruct their movement. In this way the liquid counteracts during the flow through capillary, the passing of which requires the pressure, expressed by equations (4) to (6), related to both the mentioned laws. The laminar flow is therefore characterised for a certain mean velocity, making it possible to subsequently calculate the flow volume. During the laminar flowing of a real liquid through capillary vortex rings, vortical threads with the shape of concentric circles with the centres lying in the capillary axis, are formed [2-5].

2.2 Turbulent flow

The turbulent flow of liquids (and also gases) is the most widespread and also the most complex form of macroscopic movement of mass in technical equipment and systems. The laminar flow can only be maintained up to a critical mean velocity, because at higher mean velocities of the flowing liquid the perturbative influence of the vortices begins to prevail, the flow begins to change, the liquid threads begin to interlace and turbulent flow begins. During the turbulent flow, the resistance to flow, expressed as the hydraulic gradient, is not directly proportional to the mean velocity of the liquid flowing through the capillary, as in the case of laminar flow, but it increases approximately with its second power. Accordingly, for turbulent flow the

following equation is valid for the dependence of the flow velocity of the melt through the filter and the hydraulic gradient:

$$v^{n} = \frac{\Delta p}{\Delta l} \qquad (7)$$

where v is the mean velocity of the liquid flow and n is the exponent with a value approximately in the interval from 1.75 to 2.00, while for laminar flow its value is $n = 1$. Let us add, in connection with this, that the turbulent flow is not in accordance with the relations (4) and (5), which follow from the Hagen-Poiseuille law.

The turbulence occurs for high values of the dimensionless Reynolds number, when the following inequality is valid for this number:

$$\text{Re} = \frac{v \cdot d}{v} \gg 1 \qquad (8)$$

where v is the characteristic velocity of liquid flow (m s^{-1}), d/m is the characteristic length dimension of the filter capillary and v/(m^{2} s^{-1}) is the kinematic viscosity.

Unlike laminar flow, turbulent flow has a large number of degrees of freedom, which results from the random vorticular movements of a large number of particles (aggregates, clusters) of liquid, i.e., turbulent vortexes. At each point of the turbulent flow of the liquid there are turbulent vortexes in the filter, which in various places of the capillary can even be formed upstream.

The velocity profile during the laminar flow of a liquid through the capillary has an approximately parabolic distribution of velocity with a distinct maximum at the capillary axis. On the other hand, the velocity profile during turbulent flow of the same liquid through the thin capillary is not parabolic, as it was for laminar flow, but the velocity is almost constant in all the internal parts of the capillary. The exception is the thin layer of liquid at the capillary wall, in which the flow velocity sharply increases from an almost zero value, approximately in proportion to the distance from the wall. The mean velocity of the turbulent flow of the liquid through the thin tube is therefore much closer to the maximum velocity than in the case of laminar flow. The gradient of the flow velocity of the liquid in the direction from the wall of a thin tube to its axis is thus greater during turbulent flow than during laminar flow, see **Figure 1**.

When the melt of steel or ductile iron flows through the strainer or foam filter, regardless of the elemental character of the flow (laminar or turbulent), there exists for both types of filter and for both types of metallic melt, i.e., steel and cast iron, a common character of contact for the flowing metallic melt with the filter walls. The velocity of the filtered metallic melt that is in contact with the filter walls is virtually zero; therefore, the melt can penetrate into the microscopic pores of both types of filter (strainer and foam filter), to a large extent in agreement with the Darcy law, as it is expressed with equation (6). Thus, it is possible to expect on the walls of the holes of the strainer filter, as well as on the walls of
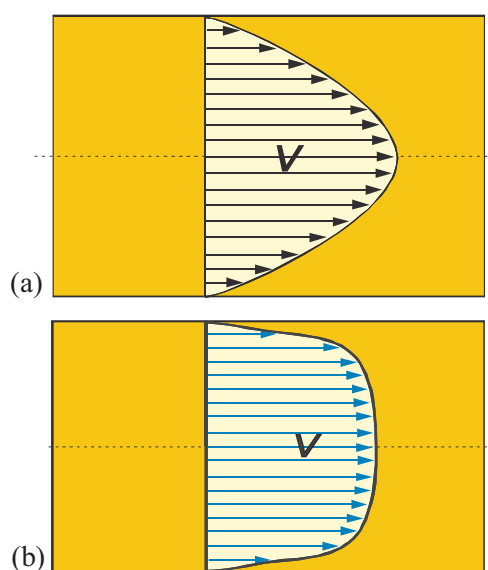
Figure 1: Profile of the velocity of laminar (a) and turbulent flow (b) of the metallic melt through a hole with a circular cross-section
Slika 1: Hitrostni profil za laminaren (a) in turbulenten (b) pretok kovinske taline skozi poro z okroglim prerezom

the irregular spaces of the foam filter, the same elementary character of physical-chemical reactions of the filtered metallic melt with the filter ceramics.

3 CONCLUSION

The hydraulic conditions have an important influence on the overall efficiency of the technology of filtration during the flowing of the melt through a ceramic filter. A knowledge of the hydraulic conditions during the flowing of the melts of steels and cast irons through ceramic filters, based on the physical regularities that govern the flow of metallic melts through the capillaries of ceramic filters, can be the basis for: a) the modelling of basic mechanisms for the flowing of melts of steels and cast irons through ceramic filters, b) a detailed explanation of the physical-chemical mechanisms of filtration occurring during the application of ceramic filters in the practice of foundries casting steels and cast irons, and c) the optimisation of the use of individual types of ceramic filters in the technology of the melting of steels and cast irons.

4 LITERATURE

[1] Horák, Z., Krupka, F., Šindelář, V. *Technická fyzika*. Teoretická knižnice inženýra [Technical physics, Engineer's Theoretical Library]. Praha, SNTL, 1961, 1436 p.
[2] Happ, J., Frohberg, M. G. *Untersuchungen zur Filtration von Eisenschmelzen*. Giessereiforschung, 23 (**1971**) 1, 1–9

[3] Flinn, R. A., Van Vlack, L. H., Colligan, G. A. *Mold-metal reactions in ferrous and nonferrous alloys*. AFS Transactions 86-09, 29–46

[4] Schmahl, J. R., Aubrey, L. S. Filtration with re-circulated silicon carbide foam: an effective means for inclusion removal in gray and nodular iron casting. AFS Transactions 93-213, 1001–1020

[5] Acosta G., F. A., Castillejos E., A. H., Almanza R., J. M., Flores V. A. Analysis of liquid flow through ceramic porous media used for molten metal filtration. Metallurgical and Materials Transactions B, 26B (**1995**), 159–171

SINTEZA MAGNETNIH NANODELCEV, FUNKCIONALIZIRANIH S TANKO PLASTJO SILIKE

SYNTHESIS OF MAGNETIC NANOPARTICLES FUNCTIONALIZED WITH THIN LAYER OF SILICA

Stanislav Čampelj[1], Darko Makovec[1], Marjan Bele[2], Miha Drofenik[1,3], Janko Jamnik[2]

[1]Oddelek za raziskavo sodobnih materialov, Institut "Jožef Stefan", Jamova 39, SI-1000 Ljubljana, Slovenija,
[2]Kemijski inštitut, Ljubljana, Hajdrihova 19, SI-1000 Ljubljana, Slovenija,
[3]Fakulteta za kemijo in kemijsko tehnologijo, Univerza v Mariboru, SI-2000 Maribor, Slovenija,
stanislav.campelj@ijs.si

V prispevku opisujemo pripravo maghemitnih nanodelcev prevlečenih s siliko. Postopek je potekal v treh ločenih stopnjah. V prvi smo delce sintetizirali s koprecipitacijo ionov Fe^{2+} in Fe^{3+}. V drugi smo delce prevlekli s citronsko kislino, da bi preprečili aglomeracijo, in jih dispergirali v vodi. Uspešnost dispergiranja smo spremljali z ugotavljanjem masnega deleža delcev, dispergiranih v vodi. Vsebnost delcev je odvisna od pH-vrednosti pri kateri se citronska kislina adsorbira na površini in koncentracije raztopljene citronske kisline. Tretja stopnja postopka je vsebovala prevlačenje nanodelcev s siliko, ki je potekalo v vodni suspenziji. Ključnega pomena za uspešno prevlačenje nanodelcev s siliko je stabilnost suspenzije nanodelcev oblečenih s citronsko kislino.

Ključne besede: maghemit, nanodelci, citronska kislina, silika, vodna suspenzija

In this paper we describe the synthesis of maghemite nanoparticles coated with silica. The process was divided into three separate steps. In first step we have synthesized particles with co-precipitation of Fe^{2+} and Fe^{3+} ions. In the second step the particles were coated with citric acid in order to prevent agglomeration and dispersed in water. The success of dispersion was determined by weight percent of dispersed particles in water. The quantity of dispersed particles depends on pH value at which the citric acid was adsorbed on the surface of particles and on the concentration of dissolved citric acid. The third step was coating the nanoparticles with silica, which took place in the water suspension. The key factor for successful coating of nanoparticles with silica is the stability of suspension of nanoparticles coated with citric acid.

Key words: maghemite, nanoparticles, citric acid, silica, water suspension

1 UVOD

V zadnjih letih se velika pozornost namenjena uporabi nanodelcev v medicini. Še posebej zanimiva je uporaba magnetnih nanodelcev, ker nanje lahko vplivamo z magnetnim poljem. Zaradi njihovih magnetnih lastnosti lahko take nanodelce spremljamo ali z njimi upravljamo na daljavo. Uporabljamo jih lahko bodisi za diagnostične namene (na primer za povečevanje kontrasta pri slikanju z NMR-tehniko) ali terapevtske tehnike, kot sta na primer magnetna hipertermija in ciljani vnos zdravilnih učinkovin[1]. Pogoj za njihovo uporabo v medicini je poleg njihove "nano"-velikosti in zadovoljivih magnetnih lastnosti tudi njihova nestrupenost in specifične površinske lastnosti. Kot magnetni material za uporabo v obliki nanodelcev v medicini se uporablja predvsem maghemit (γ-Fe_2O_3), ki velja za nestrupen material[2]. Nanodelci se za medicinske namene navadno uporabljajo v obliki suspenzij v fiziološkem mediju na vodni osnovi. Nanodelci morajo ostati dispergirani v mediju tudi ob večjih spremembah v svojem okolju, kot so na primer spremembe v ionski moči in pH-vrednosti medija. Da bi magnetne delce lahko dispergirali v tekočini, morajo izkazovati superparamagnetne lastnosti. Take lastnosti imajo pri sobni temperaturi delci magnetnega materiala, manjši od neke kritične velikosti, ki je navadno manjša od 15 nm. Superparamagnetni nanodelci zunaj magnetnega polja ne kažejo spontane magnetne polarizacije. Med njimi ni magnetnih interakcij, ki bi povzročale magnetno aglomeracijo. Stabilne koloidne suspenzije superparamagnetnih nanodelcev imenujemo tudi magnetne tekočine.

Za uporabo v medicini je treba na površino nanodelcev vezati različne biološke učinkovine. Vezavo učinkovin na površino nanodelcev dosežemo prek funkcionalizacijskega sloja molekul, vezanih na površino delcev. Te molekule zagotavljajo funkcionalne skupine za kemijsko vezavo različnih bioloških učinkovin, hkrati pa zagotavljajo stabilnost suspenzije nanodelcev. Izkaže se, da je tako za stabilnost nanodelcev v fiziološkem mediju kot tudi za učinkovitost vezave bioloških učinkovin na nanodelce ključnega pomena jakost vezi med površino in funkcionalizacijskimi molekulami.

Površina nanodelcev oksida (maghemita) je relativno inertna in navadno ne omogoča močne kovalentne vezave molekul. Zato je delce potrebno prevleči s plastjo silike, ki ima na površini silanolne OH-skupine, ki omogočajo nadaljnjo vezavo učinkovin s kovalentno vezjo. Siliko je na površino delcev mogoče vezati s sol-gel-postopkom[3,4,5] ali z Na-silikatom[6].

Pri našem delu smo sintetizirali maghemitne nanodelce in jih prekrili s tanko plastjo silike za kasnejšo funkcionalizacijo.

2 EKSPERIMENTALNO DELO

Maghemitne delce smo sintetizirali s koprecipitacijo Fe^{2+} (0,027 mol/L) in Fe^{3+} (0,023 mol/L) s koncentriranim amoniakom (25 %) pri sobni temperaturi. Postopek je potekal v dveh stopnjah. V prvi smo dvignili pH-vrednost raztopine železovih ionov na pH = 3 in vzdrževali konstantno pH-vrednost 30 min. V tej stopnji se obori $Fe(OH)_3$. V drugi stopnji smo dodali koncentriran amonijak, da smo dosegli pH = 11,6. V tej stopnji se železov hidroksid oksidira z zračnim kisikom in nastane spinelni produkt. Tako sintetizirane delce smo nato magnetno ločili in jih trikrat sprali z amoniakalno raztopino s pH > 10,5. Pri tej pH-vrednosti imajo delci na površini visok negativni naboj, kar se kaže kot visok ζ-potencial, ki preprečuje njihovo močno agregiranje. ζ-potencial sintetiziranih delcev kot tudi delcev, prevlečenih s citronsko kislino in s siliko smo določili z elektrokinetičnimi meritvami mobilnosti delcev. Meritve so bile opravljene z zetametrom (Brookhaven Instruments Corp., ZetaPALS).

Nanodelce smo karakterizirali z uporabo rentgenske praškovne difrakcije (XRD) (Bruker AXS, D4 ENDEAVOR) in presevnega elektronskega mikroskopa (TEM) (JEOL 2010F). Velikost delcev smo določili iz TEM-posnetkov in z uporabo Scherrerjeve metode, ki temelji na širitvi rentgenskih uklonov v XRD. Pri tem smo uporabljali računalniški program Diffrac[plus] Topas™.

Pred prekritjem nanodelcev s hidrolizo tetraetoksisilikana (TEOS) smo jih dispergirali v vodi, da smo omogočili prekritje posameznih delcev, in ne njihovih aglomeratov. Za dispergiranje v vodi smo delce prevlekli s citronsko kislino[7]. V mešanico vode in nanodelcev smo dodali različne količine citronske kisline (γ = 0,005–0,04 g/mL) in uravnali pH-vrednost z dodatkom amonijaka (25 %). Vrednosti pH med prekrivanjem s citronsko kislino so bile med 2 in 11. Mešanico smo segreli na 80 °C in jo intenzivno mešali 90 min. Med tem se je citronska kislina verjetno kemijsko vezala na površino nanodelcev. V naslednji stopnji procesa smo mešanico šibko aglomeriranih delcev ohladili in delce med intenzivnim mešanjem dispergirali, navadno s hkratno spremembo pH-vrednosti. Neaglomerirani delci v suspenziji so dolgoročno stabilni in se ne posedajo niti v zmernem gradientu magnetnega polja. Aglomerate smo iz suspenzije izločili s centrifugiranje na 5000 r/min, 5 min. Suspenzija po centrifugiranju je stabilna magnetna tekočina. Kot merilo za uspešnost postopka prekritja nanodelcev s citronsko kislino in njihovega dispergiranja smo uporabili vsebnost nanodelcev v stabilni magnetni tekočini. Vsebnost delcev je bila določena z žaroizgubo.

Magnetne nanodelce, dispergirane v vodi, smo prevlekli s siliko. Magnetni tekočini smo dodali etanol in TEOS (γ-Fe_2O_3 : TEOS = 1 : 23; TEOS : EtOH = 1 : 1, masna razmerja), segreli na 75 °C in pustili 24 h, da je TEOS v celoti hidroliziral. Debelino prevleke silike na nanodelcih smo kontrolirali s količino TEOS-a.

Kvaliteto prevleke silike na nanodelcih smo opazovali s visokoločljivostnim presevnim elektronskim mikroskopom (HRTEM). Izkazalo se je, da je za nastanek prevleke na posameznem delcu bistvenega pomena stabilnost njihove suspenzije, zato smo posebno pozornost namenili pripravi stabilnih magnetnih tekočin.

3 REZULTATI IN DISKUSIJA

Slika 1 prikazuje rentgenski praškovni difraktogram sintetiziranih delcev. Ta prikazuje široke uklone, ki jih lahko pripišemo spinelni fazi, tj. maghemitu.

Širjenje uklonov XRD je posledica majhnosti kristalitov. Iz širjenja XRD-uklonov je bila določena povprečna velikost kristalitov 13 nm. **Slika 2** prikazuje TEM-sliko sintetiziranih delcev. Delci, prikazani na **sliki 2**, so dobro kristalizirani in imajo ozko porazdelitev velikosti. Povprečna velikost, izračunana s **slike 2**, je
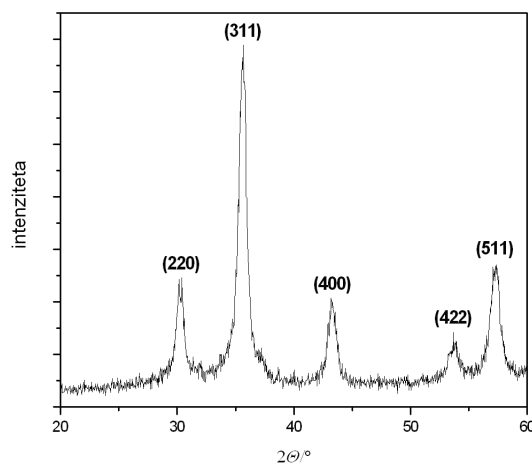
Slika 1: XRD sintetiziranih delcev
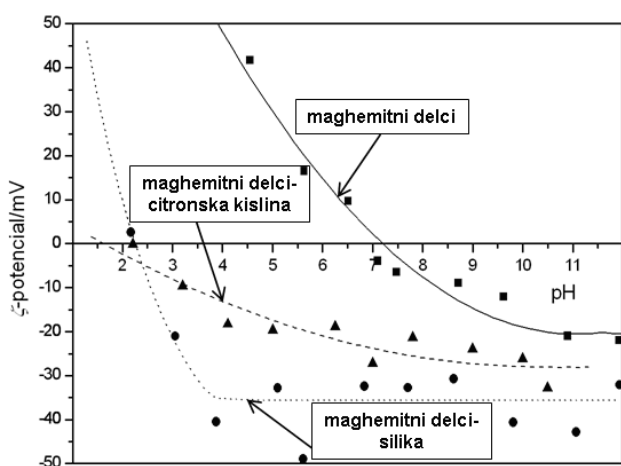**Figure 1:** XRD of synthesized particles
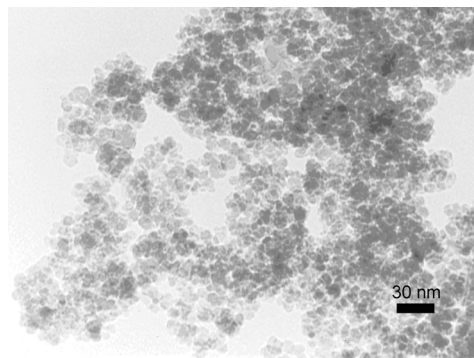
Slika 2: TEM slika sintetiziranih delcev
Figure 2: TEM image of synthesized particles

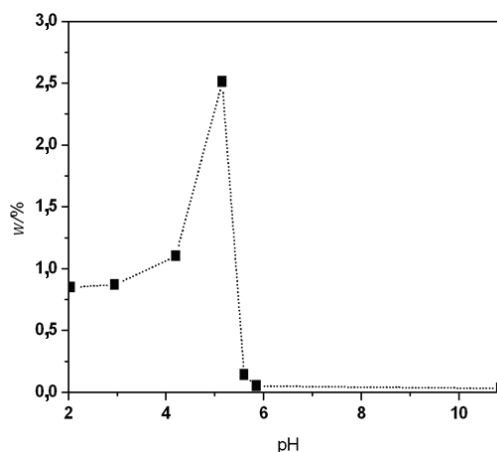13,7 ± 2,9 nm, kar se dobro sklada z velikostjo, določeno z XRD.

Delci so po sintezi aglomerirani in kot taki neprimerni za prevlačenje s siliko. Za prevlačenje s siliko je treba preprečiti aglomeracijo delcev, torej pripraviti stabilno suspenzijo v vodi. To se lahko doseže elektrostatsko, sterično ali elektrosterično. V našem primeru smo aglomeracijo preprečili z vezavo citronske kisline na površino. Kislina, vezana na površini, sterično preprečuje aglomeracijo nanodelcev, hkrati pa zagotovi na njihovi površini visok naboj, ki prispeva k elektro-statski stabilizaciji suspenzije (elektrosteričena stabiliza-cija). Uspešnost vezave citronske kisline na površino delcev je razvidna iz premika izoelektrične točke. **Slika 3** prikazuje odvisnost ζ-potenciala na nanodelcih po sintezi, delcev, prevlečenih s citronsko kislino in delcev, prevlečenih s siliko, v odvisnosti od vrednosti pH. Izoelektrična točka neprekritih delcev je pri pH = 7,2 (polna linija), izoelektrična točka delcev po prekritju s citronsko kislino pa se premakne v kislo območje pH = 2 (črtkana linija). Premik izoelektrične točke nastane zaradi spremembe na površini delcev. Pri sintetiziranih delcih so na površini kisikovi ioni. Pri delcih, prevle-čenih s citronsko kislino, pa so na površini OH-skupine citronske kisline.

Za stabilno magnetno tekočino moramo zagotoviti na površini vseh nanodelcev optimalno količino vezane citronske kisline. Merilo za stabilnost suspenzije je vsebnost magnetnih delcev v pripravljeni magnetni tekočini po centrifugiranju. Količina dispergiranih delcev je odvisna od več faktorjev, ki so povezani z vsebnostjo in vezavo citronske kisline na njihovo površino, in od pH-vrednosti, pri kateri nanodelce, prekrite s citronsko kislino, dispergiramo. Nanodelci, prekriti s citronsko kislino pri nizkih pH-vrednostih, so

Slika 4: Masni delež maghemitnih delcev v magnetni tekočini v odvisnosti od pH-vrednosti, pri kateri se je citronska kislina adsorbirala na površini nanodelcev
Figure 4: Weight percent of maghemite particles in ferrofluid as a function of pH value at which the citric acid has adsorbed on the surface of nanoparticles

se le stežka dispergirali. Izkazalo se je, da se količina nanodelcev, ki preide v stabilno suspenzijo, močno poveča, če se pH-vrednost dvigne na približno 10. Iz krivulje odvisnosti ζ-potenciala od pH-vrednosti (**slika 3**) izhaja, da s povečanjem pH-vrednosti ζ-potencial raste in s tem se povečuje stabilnost suspenzije. Delce, prevlečene s citronsko kislino, smo zato v vseh nadalj-njih poizkusih dispergirali pri pH-vrednosti 10.

Vsebnost in način vezave citronske kisline na površini nanodelcev pa je odvisna od pH-vrednosti, pri kateri je potekala adsorpcija citronske kisline na površini delcev in tudi od količine citronske kisline v suspenziji. **Slika 4** prikazuje masni delež magnetnih delcev v magnetni tekočini, določeni z žaroizgubo v odvisnosti od pH-vrednosti med adsorpcijo citronske kisline na njihovi površini. S **slike 4** je razvidno, da je največja vsebnost magnetnih delcev pri pH-vrednosti 5,2. Pri pH-vred-

Slika 3: ζ-potencial maghemitnih delcev (polna linija), maghemitnih delcev, prevlečenih s citronsko kislino (črtkana linija), in maghe-mitnih delcev, prevlečenih s siliko (pikčasta linija) v odvisnosti od pH-vrednosti
Figure 3: ζ-potential of maghemite particles (full line), maghemite particles coated with citric acid (dashed line) and maghemite particles coated with silica (dotted line) as a function of pH value
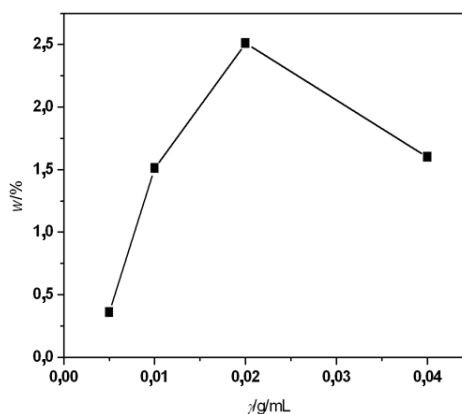

Slika 5: Masni delež maghemitnih delcev v magnetni tekočini v odvisnosti od koncentracije citronske kisline v suspenziji med procesom njene adsorpcije na površini nanodelcev
Figure 5: Weight percent of maghemite particles in ferrofluid as a function of concentration of citric acid in suspension during the adsorption of citric acid on the surface of nanoparticles
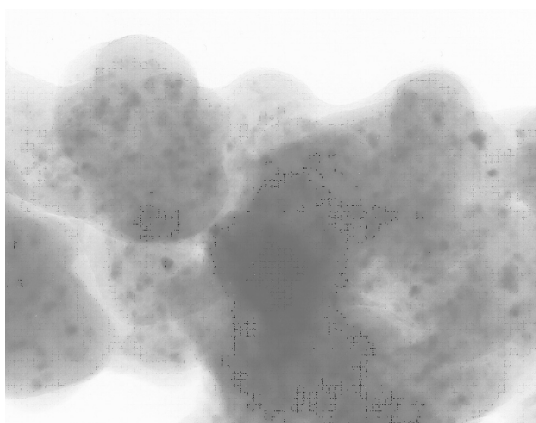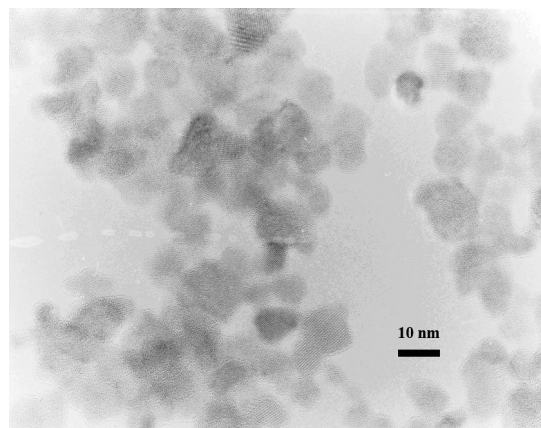
Slika 6: TEM-posnetek delcev, prevlečenih s siliko, pri nevtralni pH-vrednosti
Figure 6: TEM image of particles coated with silica at neutral pH value

Slika 7: HRTEM-posnetek maghemitnih delcev, prevlečenih s tanko plastjo amorfnega materiala
Figure 7: HRTEM image of maghemite particles coated with thin layer of amorphous material

nostih večjih od 5,2 je na površini delcev premajhen pozitiven naboj, nad pH = 7 pa je celo negativen, kar preprečuje adsorpcijo citronske kisline. Zato je količina adsorbirane kisline na površini zanemarljiva, posledica pa je majhna vsebnost magnetnih delcev v suspenziji. Pri pH-vrednostih, manjših od 5,2, je vsebnost delcev manjša zaradi senčenja naboja na površini delcev in povečane topnosti oksidnih delcev v raztopini citronske kisline.

Slika 5 prikazuje masni delež magnetnih delcev v stabilni suspenziji v odvisnosti od koncentracije citronske kisline med adsorpcijo. Ker je adsorpcija ravnotežni proces med neadsorbirano kislino, raztopljeno v vodi, in kislino, adsorbirano na površini delcev, je količina adsorbirane kisline odvisna od koncentracije kisline v raztopini. Večja kot je koncentracija citronske kisline v raztopini, večji je delež adsorbirane kisline in posledično večja količina stabilno dispergiranih delcev. Količina dispergiranih delcev se zmanjša pri koncentracijah citronske kisline, višjih od 0,02 g/mL, zaradi senčenja naboja na površini delcev. S povečanjem koncentracije ionov v suspenziji se zmanjšuje naboj na površini delcev. Ko je dosežena kritična koagulacijska koncentracija ionov, se delci začnejo agregirati.

Delce prevlečene s citronsko kislino, in dispergirane v vodi smo pri nadaljnjem delu prevlekli s siliko. Prevleka silike na nanodelcih je potekla s hidrolizo TEOS-a. Nukleacija silike mora potekati heterogeno na površini nanodelcev, in ne homogeno v sami raztopini. Zato morajo biti delci stabilno dispergirani. Za uspešno prevlačenje je ključnega pomena tudi katalizator, ki je v našem primeru amonijak. Ta je v suspenziji iz predhodnega postopka prekritja s citronsko kislino in se kaže v vrednosti pH. Optimalni pogoji za prekritje delcev so pri pH-vrednostih 10, torej pri pogojih, kjer je suspenzija najbolj stabilna in je hkrati prisotna nizka koncentracija amonijaka. Če suspenzija ni bila popolnoma stabilna, je prišlo do prekritja aglomeratov nanodelcev.

Slika 6 prikazuje TEM-posnetek delcev, oblečenih s siliko pri nevtralni pH-vrednosti. Pri pH-vrednostih okoli nevtralne točke je hidroliza potekla nehomogeno, s siliko so se prevlekli manjši aglomerati nanodelcev. Hkrati je vidna tudi nehomogena debelina silike na aglomeratih delcev, kar nakazuje, da nukleacija silike ni potekala homogeno. Prisotnost aglomeratov maghemitnih delcev nakazuje na nestabilno suspenzijo delcev med procesom prekritja.

Slika 7 prikazuje HRTEM-posnetek delcev, ki so bili prekriti z dodatkom TEOS-a 42 µL na 5 mL suspenzije maghemitnih nanodelcev, ki je imela pH-vrednost 10,1. Na površini delcev je vidna zelo tanka (≈ 1 nm) plast amorfnega materiala.

EDS-analiza posameznih delcev je pokazala relativno konstanten signal silicija, zato lahko sklepamo, da je amorfna plast na površini delcev silika. **Slika 8** prikazuje TEM-posnetek delcev, prekritih s siliko, v primeru, ko smo dodali 1,34 mL TEOS-a na 5 mL suspenzije maghemitnih nanodelcev.

Vidna je debelejša plast silike na posameznih delcih. Vsi nanodelci v vzorcu imajo na površini plast silike
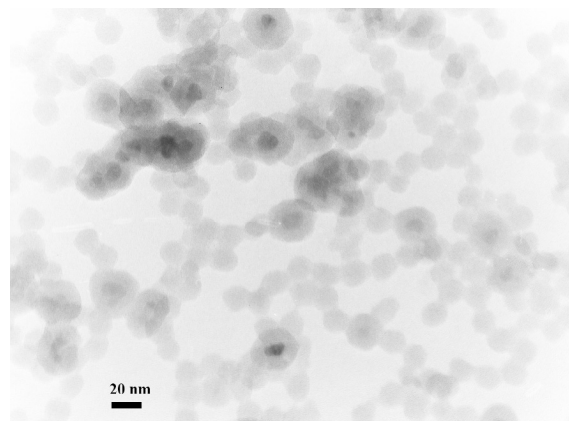
Slika 8: TEM-posnetek maghemitnih delcev, prevlečenih s siliko
Figure 8: TEM image of maghemite particles coated with silica

debelo približno 10 nm. Poleg prekritih maghemitnih delcev je v vzorcu tudi veliko majhnih nanodelcev same silike. Sestava vzorca kaže, da je prišlo do hidrolize TEOS-a ne samo na površini delcev, vendar tudi s homogeno nukleacijo silike v raztopini. Rezultat kaže, da je uporabljeni način prekritja nanodelcev primeren, treba pa bo še optimizirati pogoje, da bi se znebili delcev silike, ki ni prisotna kot prevleka na maghemitnih nanodelcih.

4 SKLEP

Uporabljena metoda prekritja superparamagnetnih nanodelcev s siliko se je izkazala za učinkovito. Ključnega pomena za uspešno prekrivanje posameznih nanodelcev je stabilnost na vodi osnovanih magnetnih tekočin. Sama metoda še ni optimizirana, saj so poleg maghemitnih delcev prekritih s siliko prisotni tudi delci silike, ki ni prisotna kot prevleka na maghemitnih nanodelcih.

5 LITERATURA

[1] I. Šafařík, M. Šafaříkova, Monatshefte für Chemie, 133 (**2002**), 737–759

[2] U. Häfeli, W. Schüt, J. Teller, M. Zborowski, Scientific and clinical applications of magnetic carriers, Plenum Press, New York, 1997

[3] W. Stöber, A. Fink, J. Colloid Interface Sci., 26 (**1968**), 62–69

[4] A. Lu, Y. Yin, B. T. Mayers, Y. Xia, Nanoletters, 2 (**2002**), 183–186

[5] Q. Liu, Z. Xu, J. A. Finch, R. Egerton, Chemical materials, 10 (**1998**), 3936–3940

[6] X. Liu, J. Xing, Y. Guan, G. Shan, H. Liu, Colloids surf. A, 238 (**2004**), 127–131

[7] Y. Sahoo, A. Goodarzi, M. T. Swihart, T. Y. Ohulchanskyy, N. Kaur, E. P. Furlani, P. N. Prasad, J. Phys. Chem. B, 109 (**2005**), 3879–3885